DEPARTMENT OF MECHANICAL ENGINEERING
COLLEGE OF ENGINEERING & TECHNOLOGY
OLD DOMINION UNIVERSITY
NORFOLK, VIRGINIA 23529

NUMERICAL SIMULATION OF SHOCK-INDUCED COMBUSTION PAST BLUNT BODIES USING SHOCK-FITTING TECHNIQUE

By

J.K. Ahuja, Graduate Research Assistant

D.J. Singh, Senior Research Scientist
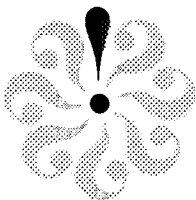
and

S.N. Tiwari, Principal Investigator

Progress Report
For the period ended June 30, 1994

Prepared for
National Aeronautics and Space Administration
Langley Research Center
Hampton, VA 23681-0001

**Submitted by the
Old Dominion University Research Foundation
P.O. Box 6369
Norfolk, VA 23508-0369**

August 1994

FOREWORD

This is a progress report on the research project, "Analysis and Computation of Internal Flow Field in a Scramjet Engine," for the period ended June 30, 1994. During this period attention was directed to "Numerical Simulation of Shock-Induced Combustion Using Shock-Fitting Technique." Important results of this study were presented at the 30th AIAA/ASME/SAE/ASEE Joint Propulsion Conference, Indianapolis, IN, June 27–29, 1994; AIAA Paper No. 94–3100, June 1994 (see Appendix A).

APPENDIX REMOVED — DOCUMENT EVALUATOR

LIST OF FIGURES

INTRODUCTION

One of the propulsion concepts for hypersonic vehicles is the proposed Oblique Detonation Wave Engine ([1–3]). In this concept, an oblique shock wave in the combustor is employed to increase the temperature of premixed fuel and air to a point where chemical reaction can start. It can be utilized to provide a smaller, light weight engine or to provide a higher payload capability for a given vehicle weight.

In the past, many researchers have conducted ballistic range experiments to study supersonic combustion/detonation. In these experiments, projectiles were fired in different fuel-air mixtures, and detonation structures around the projectiles were recorded. Every gas mixture has a detonation wave velocity known as Chapman-Jouget (C-J) velocity, which is characteristic of the mixture. If the velocity of the projectile is above the C-J velocity of the reactive mixture, the free-stream velocity is referred to as overdriven. On the other hand, if the projectile velocity is lower than the C-J velocity, the free-stream velocity is referred to as underdriven. The detonation wave structure is highly unstable for projectile velocities less than the C-J velocity of the mixture and for a particular projectile diameter. If the projectile is flying above the C-J velocity of the gas mixture, the detonation or reaction front structure shows a coupled shock-deflagration system near the stagnation line of the body. These two fronts separate from each other as one moves away from the stagnation line. The separation between the two fronts occurs as soon as the velocity component normal to the bow shock is equal to the detonation velocity. The separation between the bow shock and the reaction front is called the induction zone. In 1972 Lehr [4] conducted a detailed experimental study for a wide range of projectile shapes and combustible mixtures. The projectile shapes tested included not only spheres but cones, bi-cones, and flat-nose projectiles. The mixtures included hydrogen-air, hydrogen-oxygen, methane-air, and methane-oxygen. Ballistic range shadowgraph pictures for Mach 5.11 and Mach 6.46 from Lehr's experiments are shown in Figs.1 and 2, respectively. In both cases, a free-stream temperature of 292 K and a pressure of 42663.2 N/m^2 (320 mm of Hg) is used along with a

stoichiometric mixture of hydrogen-air. The projectile diameter was 15 mm. At these conditions the C-J Mach number of the mixture is 5.11. Figure 1 shows two discontinuities separated from each other. The outer front is the bow shock and the inner front is the reaction front produced by ignition of the heated H_2-air mixture. The separation between the two is minimum near the stagnation point and increases as the shock curves around the body, due to increase in induction distance (decrease in post shock temperature) away from the stagnation zone. A close examination of the shadowgraphs reveals that as the flow crosses the bow shock, the color changes from light to dark, indicating an increase in density. But, as the flow crosses the reaction front, the color changes from dark to light, indicating a decrease in density across the reaction front. This is due to a large release of energy across the reaction front, causing an increase in the temperature; since the pressure remains relatively constant, the density must decrease. Another interesting feature is the presence of corrugation in the reaction front. These corrugations are caused by the pulsation of the reaction front. The frequency of this pulsation was determined to be 1.96 MHz [5]. Figure 2 is for the Mach 6.46 case, and it is seen that the reaction front is coupled with the shock near the stagnation line and up to about 60–65 degree body angle from the stagnation line. This is because of a very high post-shock temperature at Mach 6.46 that causes the induction zone to become so narrow that it appears that the two fronts are merged with each other. Decoupling begins further downstream from the stagnation line when the post-shock temperature starts decreasing and, therefore, the induction distance increases. Further, both the bow shock and the reaction fronts are smooth without any visible instabilities. Thus for an overdriven case of Mach 6.46, the instabilities have disappeared. References [4,5] show other underdriven cases where it has been shown that the instabilities in the reaction front become more pronounced as we reduce the projectile velocity lower than the C-J velocity of the mixture. In all these cases the projectile diameter was fixed as 15 mm.

McVey and Toong [6] also conducted similar experiments where projectiles were fired into lean acetylene-oxygen and stoichiometric hydrogen-air mixtures. They proposed the wave

interaction model to explain the instabilities in the structure of the detonation wave. Their model explains how compression waves can be formed when a new reaction front develops in the induction zone between the normal segment of the bow shock and the original reaction front. These compression waves lead to a cyclic process which is compatible with most of the observed features of the flow. However, the strength of the compression waves remained unresolved in their wave-interaction model, which is an important factor in determining if such a model is physically possible. Alpert and Toong [7] included the effect of the strength of the compression waves and proposed a modified form of the wave-interaction model.

Several researchers [8–20] have attempted to numerically simulate Lehr's ballistic range experiments [4]. Wilson et al. [8] conducted a detailed numerical investigation of the shock-induced combustion phenomena. They used Euler equations and a 13–species and 33–reactions chemistry model. They showed the validity of the reaction models and the importance of grid resolution needed to properly model the flow physics. Highly resolved calculations for Lehr's Mach 5.11 and Mach 6.46 cases with adaptive grids were also performed. The calculations were not time accurate and, therefore, the unsteady behavior was not captured. However, for cases lower than Mach 5.11, they could successfully capture the instabilities.

Sussman et al. [9–10] also studied the instabilities in the reaction front for a Mach number of 4.79. They also used Euler equations and a 13–species and 33–reactions chemistry model. They proposed a new formulation based on logarithmic transformation, which greatly reduces the number of grid points needed to properly resolve the reaction front. The unsteady case was successfully simulated; however, the frequency was slightly underpredicted.

Matsuo and Fujiwara [11–12] have studied the instabilities of shock-induced combustion around an axisymmetric blunt body. They used Euler equations and a simplified two-step chemistry model. They investigated the growth of periodic instabilities by a series of simulations with various tip radii and showed that these periodic instabilities are related to shock-standoff distance and induction length. They proposed a new model based on McVey and Toong's model

3

[6]. The instabilities in the reaction front were explained by their model.

Ahuja et al. [13–14] and Singh et al. [15] used the Navier-Stokes equations with 7-species and 7-reactions [13–14] and 9–species and 18–reactions [15] H_2-air reaction model to simulate Lehr's Mach 5.11 and 6.46 cases using the shock-capturing method. The Mach 5.11 case was found to be unsteady while the Mach 6.46 case was macroscopically stable. The frequency of oscillations was found to be in good agreement with the experimental frequency.

The key parameters for the triggering of instabilities has been identified by various parametric studies [16]-[18]. Matsuo and Fujiwara [16] and Ahuja and Tiwari [17] showed that an underdriven case, which shows instabilities in the reaction front, can be made stable by having an appropriately small size projectile and an overdriven case can be made unstable by having a large size projectile. Kumar and Singh [18] concluded that the key parameters for triggering these instabilities were projectile velocity, activation temperature, projectile nose radius, reaction rate constant, and heat release.

Tivanov and Rom [19] conducted an analytical study based on an energy equation and a chemical rate equation for the flow of a detonable gas mixture over a blunt body. They evaluated the conditions for the stability of the detonation process and the appearance of the oscillations. The frequency of oscillations matched very well with the experimental data.

Matsuo et al. [20] simulated the regular and large disturbance regime cases of Reugg and Dorsey [21] using two-step chemistry model. With a series of simulations the large disturbance regime was explained with Alpert and Toong's model. Their results revealed that the intensity of heat release was a key parameter in determining the regime of the unsteady flow. Flow features of the unsteady combustion with low-frequency and high-amplitude oscillation, known as large-disturbance regimes, are reproduced when the concentration of the heat release is very high. For moderately high heat release, a high-frequency, low-amplitude periodic unsteadiness that belongs to regular regimes was observed.

In problems like shock-induced combustions where physical instabilities are present, the

shock-capturing methods will smear some of the instabilities. Thus shock-capturing methods, when used in complicated problems of practical interest, would not reproduce many of the intricate flow features. On the other hand, in the shock-fitting approach, one knows the precise location of the discontinuity which acts as one of the boundaries of the flow field, across which Rankine-Hugoniot conditions are applied. This approach avoids taking differences across the shock and the smearing of the shock that occur in the shock-capturing method. There are some obvious advantages of shock fitting over shock capturing. Shock fitting requires far less grid points compared to shock capturing. In shock-capturing the bow shock becomes a smeared shock surface and, requires more grid points for the extension of the grid in the free-stream region. This adds to the savings in computational time in shock fitting as compared to shock capturing. Since very small dissipation is needed in shock fitting, the intricate details of the flow can be reproduced, as the dissipation does not smear the important flow features.

The present study investigates, in detail, the shock-induced combustion phenomena for a premixed stoichiometric H_2-air mixture flow at hypersonic speeds (Mach 5.11 and 6.46), using the shock-fitting technique past a 15 mm spherical projectile. These are the first such simulations done with shock fitting for the ballistic range experiments. The analysis is carried out using the axisymmetric version of the SPARK2D code [22] with shock-fitting capability, which incorporates a seven-species, seven-reactions combustion model for hydrogen-air mixtures.

BASIC GOVERNING EQUATIONS

The physical model for analyzing the flow field is described by the Navier-Stokes and species continuity equations. For two-dimensional axisymmetric flows, these equations are expressed in physical coordinates as

$$\frac{\partial U}{\partial t} + \frac{\partial F}{\partial x} + \frac{\partial G}{\partial y} \;=\; H \tag{1}$$

5

where vectors U, F, G, and H are written as

$$U = \begin{bmatrix} \rho \\ \rho u \\ \rho v \\ \rho E \\ \rho f_i \\ \cdot \\ \cdot \end{bmatrix}$$

$$F = \begin{bmatrix} \rho u \\ \rho u^2 - \sigma_x \\ \rho u v - \tau_{xy} \\ (\rho E - \sigma_x)u - \tau_{xy}v + q_x \\ \rho f_i(u + \tilde{u}_i) \\ \cdot \\ \cdot \end{bmatrix}$$

$$G = \begin{bmatrix} \rho v \\ \rho u v - \tau_{xy} \\ \rho v^2 - \sigma_y \\ (\rho E - \sigma_y)v - \tau_{xy}u + q_y \\ \rho f_i(v + \tilde{v}_i) \\ \cdot \\ \cdot \end{bmatrix}$$

$$H = \frac{1}{y} \begin{bmatrix} \rho v \\ (\rho v u + \tau_{xy}) \\ \rho v^2 + \tau_{yy} - \tau_{\theta\theta} \\ (\rho E + p + \tau_{yy})v + \tau_{xy}u + q_y \\ \omega_i \\ \cdot \\ \cdot \end{bmatrix}$$

The other terms appearing in vectors F, G, and H are defined as

$$\sigma_x = -p + 2\mu\frac{\partial u}{\partial x} + \lambda\nabla.u \tag{2}$$

$$\sigma_y = -p + 2\mu\frac{\partial v}{\partial y} + \lambda\nabla.u \tag{3}$$

$$\tau_{xy} = \mu\left[\frac{\partial u}{\partial y} + \frac{\partial v}{\partial x}\right] \tag{4}$$

$$\tau_{yy} = -\frac{2}{3}\mu\left(2\frac{\partial v}{\partial y} - \frac{v}{y} - \frac{\partial v}{\partial x}\right) \tag{5}$$

6

$$\tau_{\theta\theta} = -\frac{2}{3}\mu\left(2\frac{v}{y} - \frac{\partial v}{\partial y} - \frac{\partial u}{\partial x}\right) \tag{6}$$

$$q_x = -k\frac{\partial T}{\partial x} + \rho\sum_{i=1}^{N_s} h_i f_i \tilde{u}_i \tag{7}$$

$$q_y = -k\frac{\partial T}{\partial y} + \rho\sum_{i=1}^{N_s} h_i f_i \tilde{v}_i \tag{8}$$

$$p = \rho R_u T\sum_{i=1}^{N_s}\frac{f_i}{M_i} \tag{9}$$

$$h_i = h_i^R + \int_{T^R}^{T} C_{p_i} dT \tag{10}$$

$$\frac{C_{p_i}}{R_i} = A_i + B_i T + C_i T^2 + D_i T^3 + E_i T^4 \tag{11}$$

The coefficients A_i, B_i, C_i, D_i, and E_i for each species is found by a curve fit of the data tabulated in reference 26.

In Eq. (1) only (N_s—1) species equations need to be considered in the formulation since the mass fraction of the species is prescribed by satisfying the constraint equation

$$\sum_{i=1}^{N_s} f_i = 1 \tag{12}$$

The specific heat at constant pressure for each species is prescribed in Eq. (11) by a fourth-order polynomial in temperature. The binary diffusion equation for the diffusion velocity of the ith species

$$\tilde{u}_i = \tilde{u}_i i + \tilde{u}_j j \tag{13}$$

7

is as follows:

$$\nabla X_i = \sum_{j=1}^{N_s} \left(\frac{X_i X_j}{D_{ij}} \right) (\tilde{u}_j - \tilde{u}_i)$$
$$+ (f_i - X_i) \left(\frac{\nabla p}{p} \right) \tag{14}$$

It may be noted that this equation has to be applied only to (N_s-1) species. The diffusion velocity for the remaining species is prescribed by satisfying the constraint equation $\sum_{i=1}^{N_s} f_i \tilde{u}_i = 0$, which ensures the consistency. In Eq. (14), it has been assumed that the body force vector per unit mass is negligible. In addition, thermal diffusion is considered to be negligible when compared with the binary diffusion coefficient.

CHEMISTRY AND THERMODYNAMIC MODELS

Chemical reaction rate expressions are usually determined by summing the contributions from each relevant reaction path to obtain the total rate of change of each species. Each path is governed by a law of mass action expression in which the rate constants can be determined from a temperature-dependent Arrhenius expression. In vector H, the term $\omega_i = M_i C_i$ represents the net rate of production of species i in all chemical reactions and is modeled as follows :

$$\sum_{i=1}^{N_s} \nu'_{ji} S_i \rightleftharpoons \sum_{i=1}^{N_s} \nu''_{ji} S_i \; ; j = 1, ... N_r \tag{15}$$

$$\omega_i = M_i \sum_{j=1}^{N_r} \left(\nu''_{ji} - \nu'_{ji} \right) \left[\kappa_{f_j} \prod_{m=1}^{N_s} C_m^{\nu'_{jm}} - \kappa_{b_j} \prod_{m=1}^{N_s} C_m^{\nu''_{jm}} \right] \tag{16}$$

where Eq.(15) is a representation of an N_r-step chemical reaction, and Eq.(16) is the production rate for the ith species as determined from the law of mass action. The reaction constants κ_{fj} and κ_{bj} are calculated from the following equations

$$\kappa_{fj} = A_j T^{\alpha j} exp \left(\frac{-\epsilon_j}{R_u T} \right) \; ; j = 1, ... N_r \tag{17}$$

$$\kappa_{bj} = \frac{\kappa_{f_j}}{\kappa_{eq_j}} \; ; j = 1, ... N_r \tag{18}$$

8

The equilibrium constant appearing in Eq.(18) is given by

$$\kappa_{eq_j} = \left(\frac{1}{R_u T}\right)^{\Delta n_j} exp\left(\frac{-\Delta G_{f_j}}{R_u T}\right) \; ; j = 1, ...N_r \tag{19}$$

where

$$\Delta n_j = \sum_{i=1}^{N_s} \nu_{ji}'' - \sum_{i=1}^{N_s} \nu_{ji}' \; ; j = 1, ...N_r \tag{20}$$

$$\Delta G_{R_j} = \sum_{i=1}^{N_s} \nu_{ji}'' g_i - \sum_{i=1}^{N_s} \nu_{ji}' g_i \; ; j = 1, ...N_r \tag{21}$$

$$\frac{g_i}{R_i} = A_i T(1 - lnT) - \left(\frac{B_i}{2}\right)T^2 - \left(\frac{C_i}{6}\right)T^3$$
$$- \left(\frac{D_i}{12}\right)T^4 - \left(\frac{E_i}{20}\right)T^5 + F_i - G_i T \; ; i = 1, ...N_s \tag{22}$$

The forward rate for each reaction is determined from Eq.(17) which is based on the Arrhenius law. The appropriate constants $A_j, \alpha_j,$ and ϵ_j for the H_2—air reaction system can be found in [23]. The reverse rate is then calculated from Eq.(18).

The hydrogen-air combustion mechanism used in this work is based on the Jachimowski hydrogen-air model [23] which uses seven species and seven reactions. The species are N_2, O_2, H_2, OH, H_2O, O, and H. Each of the seven reactions can proceed in the forward and backward directions. The reactions are

1) $O_2 + H_2 \rightleftharpoons OH + OH$

2) $O_2 + H \rightleftharpoons OH + O$

3) $H_2 + OH \rightleftharpoons H_2O + H$

4) $H_2 + O \rightleftharpoons OH + H$

5) $OH + OH \rightleftharpoons H_2O + O$

6) $OH + H + M \rightleftharpoons H_2O + M$

7) $H + H + M \rightleftharpoons H_2 + M$

The stoichiometric chemical reaction for a hydrogen-air system can be written as

$2H_2 + O_2 + 3.76N_2 \rightarrow 2H_2O + 3.76N_2$
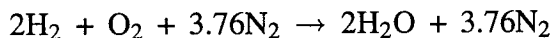
For a blunt body moving through a reactive mixture at hypersonic speeds, the temperature of

9

the fuel-air mixture after the bow shock is sufficiently high to initiate the reaction. Once the ignition starts, chemical energy is released and the reaction front is formed. In the induction zone, the temperature and pressure remain relatively constant at the post-shock conditions, while the concentrations of radicals build up very rapidly.

METHOD OF SOLUTION

The governing equations of motion are transformed from physical space (x,y) to the computational domain (ξ, η) by the following relations

$$\tau = t$$

$$\xi = \xi(t, x, y) \tag{23}$$

$$\eta = \eta(t, x, y)$$

The final form of the governing equation in the computational domain with time-dependent terms is given by

$$\frac{\partial \hat{U}}{\partial \tau} + \frac{\partial \hat{F}}{\partial \xi} + \frac{\partial \hat{G}}{\partial \eta} = \hat{H}$$

In expanded form, the above equation can be written as

$$\left(\underbrace{\overbrace{J^{-1}U}^{\hat{\mathbf{U}}}}_{} \right)_\tau + \left(\overbrace{[\{-x_\tau y_\eta + x_\eta y_\tau\} U + y_\eta F - x_\eta G]}^{\hat{\mathbf{F}}} \right)_\xi$$

$$+ \left(\overbrace{[\{x_\tau y_\xi - x_\xi y_\tau\} U - y_\xi F + x_\xi G]}^{\hat{\mathbf{G}}} \right)_\eta$$

$$= J^{-1}H + \overbrace{\underbrace{[U\{-x_\tau y_\eta + x_\eta y_\tau\}_\xi + U\{x_\tau y_\xi - x_\xi y_\tau\}_\eta]}_{\text{GCL TERMS}}}^{\hat{\mathbf{H}}}$$

$$+ \overbrace{\underbrace{[F(y_\eta)_\xi - F(y_\xi)_\eta - G(x_\eta)_\xi + G(x_\xi)_\eta]}_{\text{GCL TERMS}}}^{\hat{\mathbf{H}}} \tag{24}$$

Those terms which add to zero analytically, but numerically are not zero, are referred to as GCL (Geometric Conservation Law correction) terms in Eq. 24 above.

BOUNDARY CONDITIONS

The flow conditions behind the bow shock are determined by Rankine-Hugoniot relations. The shock boundary is allowed to move until it reaches a steady state position. Figure 3 shows the coordinate transformation used in the shock-fitting procedure where the following notations are employed: Let $\vec{V_1}$ represent the vector component of the fluid velocity normal to, and measured with respect to, the moving shock. Therefore, one may express

$$
\begin{aligned}
\vec{V_1} &= \left\{ \left[\vec{V}_\infty - \vec{U}_s \right] \cdot \vec{n} \right\} \vec{n} \\
&= \left\{ \left(v_\infty \vec{i_r} \cdot \vec{n} + u_\infty \vec{i_\theta} \cdot \vec{n} - \vec{U}_s \cdot \vec{n} \right) \cdot \vec{n} \right\}
\end{aligned}
\tag{25}
$$

Consequently, the magnitude of the shock velocity in the direction normal to the body (i.e., along the radius) is given by

$$
r_{s_t} = V_1 \left[1 + \left(\frac{r_{s\theta}}{r_s} \right)^2 \right]^{1/2} + v_\infty - u_\infty \left(\frac{r_{s\theta}}{r_s} \right)
\tag{26}
$$

The derivative $r_{s_\theta}^n$ which appears in Eq. (26) is evaluated by using the second-order central difference formula as

$$
r_{s_{\theta(j)}}^n = \frac{\left(r_{s_{\theta(j+1)}}^n - r_{s_{\theta(j-1)}}^n \right)}{2\Delta\theta} \qquad (2 \le j \le nny - 1)
\tag{27}
$$

At the beginning of the predictor step, the shock wave radial distance is computed from the Euler predictor equation

$$
r_{s(t+\Delta t)} = r_{s(t)} + \Delta t \frac{\partial r_s}{\partial t}
$$

or

$$
r_s^{\overline{n+1}} = r_s^n + \Delta t \, r_{s_t}^n
\tag{28}
$$

11

Therefore,

$$\vec{V}_1 = V_1 \cdot \vec{n}$$

(29)

$$= v_1 \vec{i}_r + u_1 \vec{i}_\theta$$

where v_1 =component of fluid velocity V_1 normal to the body (i.e., along $\vec{i}_r$ direction) and u_1= component of the fluid velocity V_1 tangential to the body (i.e., along $\vec{i}_\theta$ direction) Therefore,

$$u_1 = -\frac{\left(\frac{r_{s\theta}}{r_s}\right)}{\left[1 + \left(\frac{r_{s\theta}}{r_s}\right)^2\right]} \left[r_{s_t} - v_\infty + u_\infty \left(\frac{r_{s\theta}}{r_s}\right)\right]$$

(30)

and

$$v_1 = \left[r_{s_t} - v_\infty + u_\infty \left(\frac{r_{s\theta}}{r_s}\right)\right] \frac{1}{\sqrt{1 + \left(\frac{r_{s\theta}}{r_s}\right)^2}}$$

(31)

Let u_{1_s} = velocity component tangent to the shock (i.e., in $\vec{s}$ direction) and v_{1_n} = velocity component normal to the shock (i.e., in $\vec{n}$ direction). Then by applying shock jump conditions, we have

$$\rho_1 v_{1n} = \rho_2 v_{2n}$$

(32)

Since tangential velocity is preserved, then

$$u_{2s} = u_{1s}$$

(33)

Let $\vec{V}_2$ = resultant velocity after the shock with respect to shock coordinates. Therefore,
$\vec{V}_2 = v_{2n}\vec{n} + u_{2s}\vec{s}$
The component of $\vec{V}_2$ along $\vec{i}_\theta$ (i.e., tangent to the body) is given by

$$u_2 = \vec{V}_2 \cdot \vec{i}_\theta$$

(34)

Similarly the component of $\vec{V}_2$ along $\vec{i}_r$ (i.e., normal to the body) is given by

$$v_2 = \vec{V}_2 \cdot \vec{i}_r$$

(35)

Therefore,

$$u_2 = U_\infty - \left(1 - \frac{\rho_1}{\rho_2}\right) \times \frac{\left[r_{s_t} - v_\infty + U_\infty \left(\frac{r_{s\theta}}{r_s}\right)\right]\left(\frac{r_{s\theta}}{r_s}\right)}{\left[1 + \left(\frac{r_{s\theta}}{r_s}\right)^2\right]}$$

(36)

Similarly,

$$v_2 = v_\infty + \left(1 - \frac{\rho_1}{\rho_2}\right) \times \frac{\left[r_{s_t} - v_\infty + U_\infty \left(\frac{r_{s_\theta}}{r_s}\right)\right]}{\left[1 + \left(\frac{r_{s_\theta}}{r_s}\right)^2\right]} \tag{37}$$

Pressure behind the shock is obtained from the MacCormack scheme at the predictor level. Once the pressure is known behind the shock, the normal component of the flow velocity ahead of the shock (measured with respect to shock) can be related to the pressure behind the shock by manipulating the oblique shock relations which are

$$\rho_1 v_1 = \rho_2 v_2$$

$$p_1 + \rho_1 v_1^2 = p_2 + \rho_2 v_2^2$$

$$u_1 = u_2 \tag{38}$$

$$h_1 + \frac{V_1^2}{2} = h_2 + \frac{V_2^2}{2}$$

where V_1 and V_2 are resultant velocities. Manipulating these equations gives

$$v_1 = \sqrt{\left(\frac{\gamma + 1}{2}\right) \frac{p_1}{\rho_1} \left[\frac{p_2}{p_1} + \frac{\gamma - 1}{\gamma + 1}\right]} \tag{39}$$

and

$$\frac{\rho_2}{\rho_1} = \frac{\frac{\gamma+1}{\gamma-1}\frac{p_2}{p_1} + 1}{\frac{\gamma+1}{\gamma-1} + \frac{p_2}{p_1}}$$

$$= \frac{\frac{p_2}{p_1} + \frac{\gamma-1}{\gamma+1}}{1 + \frac{\gamma-1}{\gamma+1}\frac{p_2}{p_1}} \tag{40}$$

Equations (28), (36), (37), (39), and (40), when written in the notations of the advanced time level in terms of the preceding time level, can be written as

$$r_s^{\overline{n+1}} = r_s^n + \Delta t\, r_{s_t}^n \tag{41}$$

$$V_{nnx,j}^{\overline{n+1}} = \sqrt{\left(\frac{\gamma + 1}{2}\right) \frac{p_\infty}{\rho_\infty} \left[\frac{p_{nnx,j}^{\overline{n+1}}}{p_\infty} + \frac{\gamma - 1}{\gamma + 1}\right]} \tag{42}$$

$$\frac{\rho_{nnx,j}^{\overline{n+1}}}{\rho_\infty} = \frac{\frac{p_{nnx,j}^{\overline{n+1}}}{p_\infty} + \frac{\gamma-1}{\gamma+1}}{1 + \frac{\gamma-1}{\gamma+1}\frac{p_{nnx,j}^{\overline{n+1}}}{p_\infty}} \tag{43}$$

$$u^{\overline{n+1}}_{nnx,j} = u_\infty - \left(1 - \frac{\rho_\infty}{\rho^{\overline{n+1}}_{nnx,j}}\right)$$

$$\times \frac{\left[r^{\overline{n+1}}_{s_{t(j)}} - v_\infty + u_\infty\left(\frac{r^{\overline{n+1}}_{s_{\theta(j)}}}{r^{\overline{n+1}}_{s(j)}}\right)\right]\left(\frac{r^{\overline{n+1}}_{s_{\theta(j)}}}{r^{\overline{n+1}}_{s(j)}}\right)}{\left[1 + \frac{r^{\overline{n+1}}_{s_{\theta(j)}}}{r^{\overline{n+1}}_{s(j)}}\right]} \tag{44}$$

$$v^{\overline{n+1}}_{nnx,j} = v_\infty + \left(1 - \frac{\rho_\infty}{\rho^{\overline{n+1}}_{nnx,j}}\right)$$

$$\times \frac{\left[r^{\overline{n+1}}_{s_{t(j)}} - v_\infty + u_\infty\left(\frac{r^{\overline{n+1}}_{s_{\theta(j)}}}{r^{\overline{n+1}}_{s(j)}}\right)\right]}{\left[1 + \left(\frac{r^{\overline{n+1}}_{s_{\theta(j)}}}{r^{\overline{n+1}}_{s(j)}}\right)^2\right]} \tag{45}$$

Note i is normal to the body and varies from i=1 at the surface to i=nnx at the shock. Also j is along the body and varies from j=1 at the stagnation line to j=nny at the outflow boundary.

SOLUTION PROCEDURE

Solution procedures are followed in four steps as described below.

STEP 1 : Initial Solution

The initial conditions for this calculation are obtained by using an approximate curve fit for the location and shape of the bow shock. Newtonian pressure distribution is used at the body. The approximate curve fit of Billig [25] is used to find r_s and $r_{s\theta}$ along the shock. To find the initial conditions immediately behind the shock, the radial shock velocity r_{s_t} is set equal to zero and Eqs. (25), (42)-(45) are used. The initial flow conditions on the wall are obtained using the known wall temperature in conjunction with the pressure from the Newtonian pressure distribution. The initial flow conditions at interior grid points are obtained by assuming a linear variation between the flow conditions immediately behind the bow shock and the wall conditions.

STEP 2 : Predictor Step

At the beginning of the predictor step, the shock wave radial distance is computed from Eq.

14

(30). The pressure immediately behind the shock $\left(p_{nnx,j}^{\overline{n+1}}\right)$ is computed using the MacCormack scheme

$$
\begin{aligned}
U_{nnx,j}^{\overline{n+1}} = U_{nnx,j}^{n} &- \frac{\Delta t}{\Delta y}\left(F_{nnx,j+1}^{n} - F_{nnx,j}^{n}\right) \\
&- \frac{\Delta t}{\Delta x}\left(G_{nnx,j}^{n} - G_{nnx-1,j}^{n}\right) - \Delta t H_{nnx,j}^{n}
\end{aligned}
\tag{46}
$$

Once the pressure behind the bow shock is obtained, $V_{nnx,j}^{\overline{n+1}}$ and $\rho_{nnx,j}^{\overline{n+1}}$ can be computed from the normal shock relations given by Eqs. (42) and (43). Similarly the components of the fluid velocity behind the bow shock can be found from the oblique shock relations given by Eqs. (44) and (45). The remaining unknown $T_{nnx,j}^{\overline{n+1}}$ is calculated using the equation of state. This completes the predictor step.

STEP 3 : Corrector Step

The corrector step is similar to the predictor step except that the shock wave radial distance is evaluated using the modified Euler corrector which is

$$
r_{s(j)}^{n+1} = r_{s(j)}^{n} + \frac{\Delta t}{2}\left(r_{s_{t(j)}}^{n} + r_{s_{t(j)}}^{\overline{n+1}}\right)
\tag{47}
$$

and Eq. (46) is replaced by the MacCormack Corrector scheme in which the usual backward difference for $\partial G/\partial y$ is replaced by a forward difference given by

$$
\begin{aligned}
U_{nnx,j}^{n+1} = \frac{1}{2}&\left[U_{nnx,j}^{n} + U_{nnx,j}^{\overline{n+1}} - \frac{\Delta t}{\Delta y}\left(F_{nnx,j}^{\overline{n+1}} - F_{nnx,j-1}^{\overline{n+1}}\right)\right] \\
&- \frac{1}{2}\left[\frac{\Delta t}{\Delta x}\left(G_{nnx,j}^{\overline{n+1}} - G_{nnx-1,j}^{\overline{n+1}}\right) + \Delta t H_{nnx,j}^{\overline{n+1}}\right]
\end{aligned}
\tag{48}
$$

This completes the corrector step.

STEP 4 :

Once the calculation of boundary condition at i=nnx (i.e., after the shock) has been performed by the shock fitting method, the predictor or corrector steps are initiated at the interior grid points. All other boundary conditions are calculated after the predictor or corrector step is completed at all interior grid points.

The flow conditions along the supersonic outflow boundary (i.e., at j=nny) are determined by using a second-order extrapolation of interior grid point data.

Along the body surface the boundary conditions of no slip, zero pressure gradient, adiabatic, and non-catalytic wall were used.

RESULTS AND DISCUSSION

Numerical computations were conducted to simulate Lehr's [4,5] experimental results. The physical and free-stream conditions used in the simulations were:

$M_\infty = 5.11$ and 6.46

$P_\infty = 42732 N/m^2$

$T_\infty = 292K$

$r_n = 15\,mm$

Figure 4 shows the typical grid used in the calculation. For the Mach 5.11 case, calculations were carried out on a grid of 101×101. Due to close coupling of bow-shock and reaction front (i.e., small induction distance) at high Mach numbers, a finer grid was needed to resolve the flow field. Therefore, for Mach 6.46, a grid of 201×151 was used with 201 points in the circumferential direction and 151 points in the normal directions.

Figure 5 and 6 show the pressure contour plots for the Mach 5.11 case. The complicated wave pattern seen in Fig. 5 can be viewed as made up of two types of compression waves. One type of compression wave originates from the reaction front while the other has been reflected from the projectile body. The reflected compression wave interacts with the original compression wave and, at the point of interaction, two new waves are generated. This reflection produces the observed cell structure. The compression wave which moves towards the bow shock, overtakes it and causes the bow shock to move forward. Thus the kinks appearing on the bow shock are due to some of its structure being distorted by the compression waves. Figure 5 also reveals that these pulsations in reaction front are strong near the nose region and dissipate near the shoulder regions of the projectile. This fact is further supported by Fig. 7, which shows the numerical value of pressure contours along the complete body. From the pressure values given, it is shown that the pulsation of compression waves that originate near the stagnation line are

16

the strongest, and as one moves towards the shoulder region of the projectile, the pressure is reduced to almost atmospheric pressure.

Figure 8 shows the pressure distribution along the stagnation line. The pressure increases from free-stream pressure to 1.332 e+06 N/m^2 as the flow passes the normal shock along the stagnation line. The flow then encounters the pressure wave (see Fig. 6) which further raises the pressure to 1.375 e+06 N/m^2. The pressure then drops to 1.342 e+06 N/m^2 as it passes through the expansion wave. This pattern repeats itself as the flow encounters a series of compression and expansion waves.

To help understand the temporal nature of these instabilities, attention is now focused on the time history of physical variables along the stagnation line. Figure 9 shows the time history plot of water mass-fraction along the stagnation streamline. It shows two discontinuities. The outer discontinuity is the bow shock, which shows little kinks in the structure, and the inner discontinuity is the reaction front. The highly periodic oscillations in the reaction front that originate near the stagnation line and then spread downstream are clearly evident. The bow shock is at 0.009224 meter and the projectile surface is at 0.0075 meter (projectile surface is not shown in the figure) from the center of the blunt body. As seen from the figure, the frequency of oscillation (which is inverse of the time period) can be calculated directly from the plot. This frequency is 2.0 MHz, whereas the experimental frequency from Lehr's ballistic data for Mach 5.11 is 1.98 MHz. Also, the amplitude of the oscillations of reaction front is 8.0 e-05 meters. Figure 10 shows the water mass fraction contours. The reaction front can be seen in this figure. The instability is characterized by a regular periodic wave motion having a constant frequency and amplitude. The contour plots shown here show the spatial variation of instability at one point in time. They also show that instabilities are not restricted to the reaction front only but are convected towards the body, thus affecting the entire flow field. The reaction is complete near the body where the maximum water mass production can be seen.

Density contours are shown in Fig. 11. It clearly shows the presence of two discontinuities.

The outer discontinuity is the bow shock and the inner discontinuity is the reaction front. These two fronts can be seen separated from each other. Moving downstream the induction length increases because of lowering of post-shock temperature. The oscillations in the reaction front can be seen clearly. It is also seen that the density increases just after the shock and then decreases as the flow passes through the reaction front, in agreement with the experimental shadowgraph.

Figure 12 shows the temperature distribution along the stagnation streamline. Following a streamline into the stagnation zone, it is seen that the temperature jumps across the shock and then stays constant in the induction zone. Past the induction zone, due to the exothermic nature of the H_2-air reaction mechanism, the temperature increases rapidly reaching almost 11 times (3150 K) the free-stream value. The pulsation in the temperature can be vividly seen here. To further compare the experimental data with the numerical data, Fig. 13 shows the computed shadowgraph of the Mach 5.11 case. It is seen that the bow shock and the reaction front are separated from each other near the stagnation line, and this separation keeps increasing downstream of the stagnation line. This is what was observed experimentally also. Also, the bow shock is quite smooth with very little waviness but the reaction front clearly shows a periodic behavior. The instability is characterized by an almost regular periodic wave motion having a constant frequency, similar to that observed experimentally in Lehr's work.

By means of time history plots, a comparison of the numerical results with the wave-interaction model originally proposed by McVey and Toong [6] and further modified by Matsuo and Fujiwara [11], can be made. The essential features of this one-dimensional model are shown in Fig. 14. In order to understand how the wave interaction model fits with the numerical results, we shall have to consider Figs. (14–18) together.

Figure 15 shows the time history plot for the pressure along the stagnation streamline and Fig. 16 shows the enlarged view showing the actual numerical values of pressure. Figures 17–18 show the time history plots of density and temperature, respectively, along the stagnation streamline. By comparing the actual model shown in Fig. 14 with the x-t diagrams of pressure,

density, and temperature shown in Figs. 15–18, it is demonstrated below that the model proposed by McVey and Toong fits very well with the present numerical calculations.

As shown in Fig. 14, a contact discontinuity first approaches the original reaction front. The gases are hot on the upstream side of the contact discontinuity and comparatively cold on the lower side, as clearly seen in Fig. 18. These hot gases behind the contact discontinuity begin to react, generating compression or pressure waves that propagate both upstream and downstream, as seen in Fig. 15 and the enlarged view in Fig. 16. The compression wave which propagates upstream intersects with the bow shock and produces a contact discontinuity behind the bow shock (Figs. 17 and 18). The bow shock is stronger after the interaction and, therefore, the gas is hotter on the upstream side of the contact discontinuity. The hot gases behind the contact discontinuity reduce the induction time and create a new reaction front, thus generating another set of compression waves. At a somewhat later time, the contact discontinuity reaches the position of the original reaction front, extinguishing the reaction at this point because no more unreacted mixture exists there. The rate of energy release is effectively reduced, which generates rarefaction waves as shown in Fig. 16. The reaction front begins to recede because of increasing induction time of the colder fluid. The compression wave traveling towards the blunt body gets reflected from the body, travels back to the bow shock, and interacts with it at about the same time that the most recently created compression wave arrives at the bow shock. The compression wave and the reflected compression wave from the body interact with the bow shock, thus providing a possible mechanism for the creation of another contact discontinuity, i.e., secondary contact discontinuity. The gases, being hotter on the upstream side of the contact discontinuity, start burning again generating compression waves; the cycle is then repeated as shown in Figs. 15. and 16. Matsuo and Fujiwara also emphasized the importance of considering the reflection of the compression wave from the body in their calculations. The compression wave reflected from the blunt body may not necessarily be in phase with the compression waves created by the new energy release front. Thus, once these reflected waves interact, they cause

the flow to be not exactly periodic; however, the pulsating energy release front could still be nearly periodic.

The results for the Mach 6.46 case are now presented. This is a superdetonative case, i.e., the projectile velocity is higher than the C-J velocity of the mixture. Figure 19 shows the pressure contours as well as the wave pattern similar to Mach 5.11. When compared with Fig. 6, it is clear that the frequency of the compression waves moving towards the body and moving towards the bow shock is much higher. The bow shock and the reaction front are almost coupled with each other. Fig. 20 shows the density contours. For this case, a very small induction distance occurs as a result of the post-shock temperature remaining significantly high up to some distance downstream of the stagnation zone. Away from the stagnation line, the induction distance is increased as a result of the decreasing shock strength and post-shock temperature. The bow shock has a very crisp and smooth profile. The reaction front, which is smooth up to about 60–65 degrees from the nose region, is wrinkled with very small amplitude waves downstream. Figure 21 shows the pressure distribution along the stagnation streamline. There is a jump in pressure after the bow shock and then the pressure drops when the pressure wave meets a rarefaction wave. It increases again when it encounters another compression wave. After the energy release front, there is another jump in pressure. This pressure wave oscillates between a high value (when it encounters a compression wave) to a low value (when it encounter a rarefaction wave). Also, when compared with Fig. 8 for Mach 5.11, we see that there are more numerous oscillations in pressure for the Mach 6.46 case because of higher frequency compression waves generated. Figure 22 shows the temperature distribution along the stagnation streamline. The stagnation point temperature is 3550 K. The temperature increases abruptly as the gas encounters the bow shock. Immediately after the shock, the temperature stays constant for a short distance and then begins to increase due to exothermic reaction. Figure 23 shows the computed shadowgraph for density. The bow shock and the reaction front remain coupled with each other up to about 60–65 degrees from the stagnation streamline, as observed experimentally, and then start decoupling.

Also, the reaction front shows slight oscillations of very low amplitude. Figure 24 shows the time history plot for water mass fraction. The bow shock is at 0.00884 meters from the center of the blunt body. The distance between the bow shock and the reaction front is very small. Also, as is clear from the figure, the amplitude of oscillations of the reaction front is 2.5 e-05 meters which is quite small as compared with the Mach 5.11 case. The frequency of oscillations can be computed directly from this figure and it is found to be 2.85 MHz, which is comparable with the earlier work [14]. Thus, Mach 6.46 case is a very high frequency but very low amplitude phenomena. Experimental fundamental frequency for the Mach 6.46 case is not available.

CONCLUSIONS

A shock-fitting technique has been used to simulate the shock-induced combustion past blunt projectiles. In such problems which involve instabilities, the shock-fitting technique gives much better resolution of the flow features than the shock-capturing technique. The observed flow features have been successfully correlated with the one-dimensional wave-interaction model, and the frequency of oscillations has been matched with the experimental data as well as with earlier investigations.

REFERENCES

1. Cambier, J. L. and Adelman H., "Numerical Simulations of an Oblique Detonation Wave Engine," AIAA Paper 88–0063, January 1988.

2. White, M. E., Drummond, J. P., and Kumar, A., "Evolution and Status of CFD Techniques for Scramjet Applications," AIAA Paper 86–0160, January 1986.

3. Atamanchuk, T. and Sislian J., "On-And-Off Design Performance Analysis of Hypersonic Detonation Wave Ramjets," AIAA Paper 90–2473, July 1990.

4. Lehr, H. F., "Experiments on Shock-Induced Combustion,"Acta Astronautica, Vol. 17, September 1972, pp. 589–586.

5. Anonymous, Rapport-Bericht CO 7/73, Institut Franco-Allenmand De Recherches De Saint-Louis, Kolloquium Uber Gasdetonationen, obgehalten im ISL am 22.10.1973, ISL-

Beitrage.

6. McVey, J. B. and Toong, T. Y., "Mechanism of Instabilities of Exothermic Hypersonic Blunt-Body Flows," Combustion Science and Technology, Vol. 3, 1971, pp. 63–76.

7. Alpert, L. R. and Toong, T. Y., "Periodicity in Exothermic Hypersonic Flows about Blunt Projectiles," Acta Astronautica, Vol. 17, September 1972, pp. 539–560.

8. Wilson, G. J. and MacCormack R. W., "Modelling Supersonic Combustion Using a Fully-Implicit Numerical Method," AIAA Journal, Vol. 30, No. 4, 1992, pp. 1008–1015.

9. Sussman, M. A., "Source Term Evaluation for Combustion Modelling," AIAA Paper 93–0239, January 1993.

10. Wilson, G. J. and Sussman, M. A., "Computation of Unsteady Shock-Induced Combustion Using Logarithmic Species Conservation Equations," AIAA Journal, Vol. 31, 1993, pp. 294–301.

11. Matsuo, A. and Fujiwara T., "Numerical Simulations of Shock-Induced Combustion around an Axisymmetric Blunt Body," AIAA Paper 91–1414, June 1991.

12. Matsuo, A. and Fujiwara, T., "Numerical Investigation of Oscillatory Instability in Shock-Induced Combustion around a Blunt Body," AIAA Journal, Vol. 31, 1993, pp. 1835–1841.

13. Ahuja, J. K. and Tiwari, S. N., "Investigation of Hypersonic Shock-Induced Combustion in a Hydrogen-Air System," AIAA Paper 92–0339, January 1992.

14. Ahuja, J. K. and Tiwari, S. N., "Numerical Simulation of Shock-Induced Combustion in a Superdetonative Hydrogen-Air System," AIAA Paper 93–0242, January 1993.

15. Singh, D. J., Ahuja, J. K., and Carpenter, M. H., "Numerical Simulations of Shock-Induced Combustion/Detonation," Computing Systems in Engineering, Vol. 3, 1992, pp. 201–215.

16. Matsuo, A., Fujiwara, T., and Fujii, K., "Flow Features of Shock-Induced Combustion around Projectiles Travelling at Hypervelocities," AIAA Paper 93–0451, January 1993.

17. Ahuja, J. K. and Tiwari, S. N., "A Parametric Study of Shock-Induced Combustion in a Hydrogen-Air System," AIAA Paper 94–0674, January 1994.

18. Kumar, A. and Singh, D. J., "Unsteady Shock-Induced Combustion Past Blunt Bodies," Proceedings of the ICASE/LaRC Workshop on Transition, Turbulence, and Combustion, accepted for publication October 1993.

19. Tivanov, G. and Rom, J., "Analysis of the Stability Characteristics of Hypersonic Flow of a Detonable Gas Mixture in the Stagnation Region of a Blunt Body," AIAA Paper 93–1918, June 1993.

20. Matsuo, A., Fujii, K., and Fujiwara, T., "Computational Study of Unsteady Combustion around Projectiles with emphasis on the Large-Disturbance Oscillation," AIAA Paper 94–0764, January 1994.

21. Ruegg, F. W. and Dorsey, W., "A Missile Technique for the Study of Detonation Waves," J. Res. Natl. Bur. Std., Vol. 66C, No. 1, Jan.-Mar. 1962, pp. 51–58.

22. Drummond, J. P., Rogers, R. C., and Hussaini, M. Y., "A Detailed Numerical Model of a Supersonic Reacting Mixing Layer," AIAA Paper 86–1427, June 1986.

23. Jachimowski, C. J., "An Analytical Study of the Hydrogen-Air Reaction Mechanism with Application to Scramjet Combustion," NASA TP-2791, 1988.

24. MacCormack, R. W., "The Effect of Viscosity in Hypervelocity Impact Cratering," AIAA Paper 69–354, April-May 1969.

25. Billig, S. F., "Shock-Wave Shapes around Spherical and Cyndrical-Nosed Bodies," J. Spacecraft, Vol. 4, No. 6, 1967, pp. 822–823

26. McBridge, B. J., Heimel, S., Ehlers, J. G., and Gordon, S., "Thermodynamic Properties to $6000\,^{\circ}$K for 210 Substances Involving the First 18 Elements," NASA SP-3001, 1963.
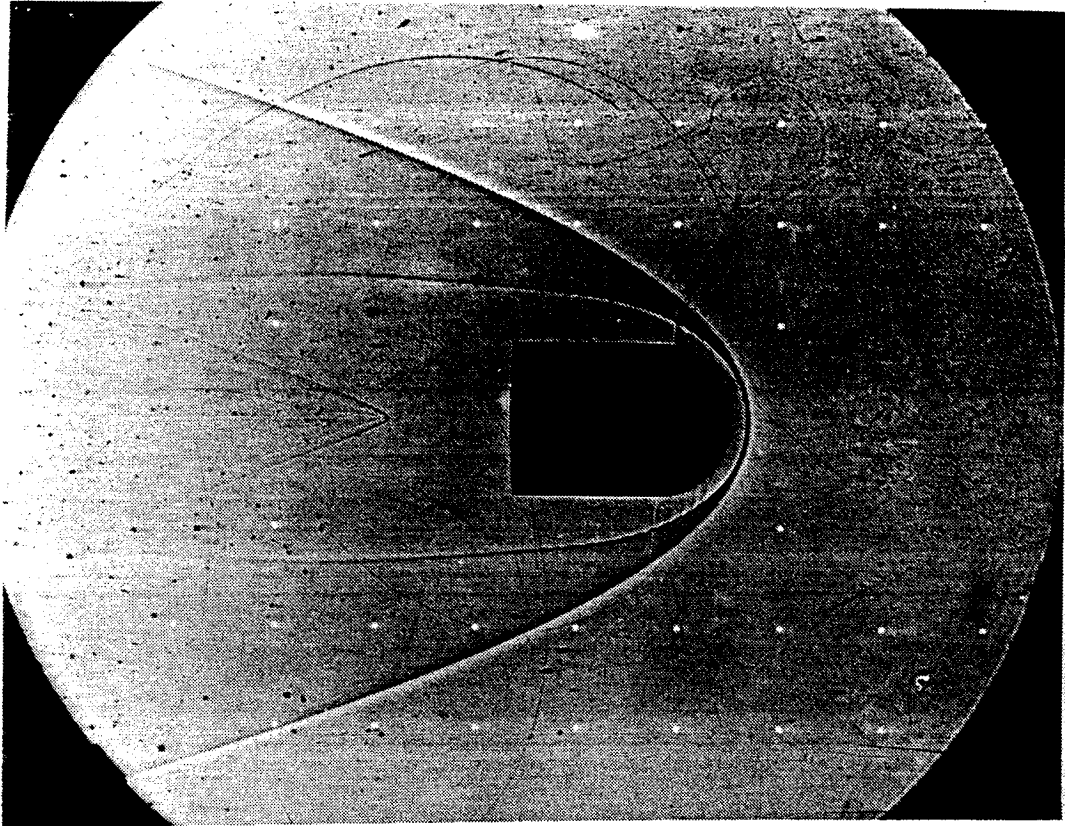
Figure 1 Shadowgraph of a spherical nose projectile moving at
Mach 5.11 into a premixed stoichiometric hydrogen-air mixture.
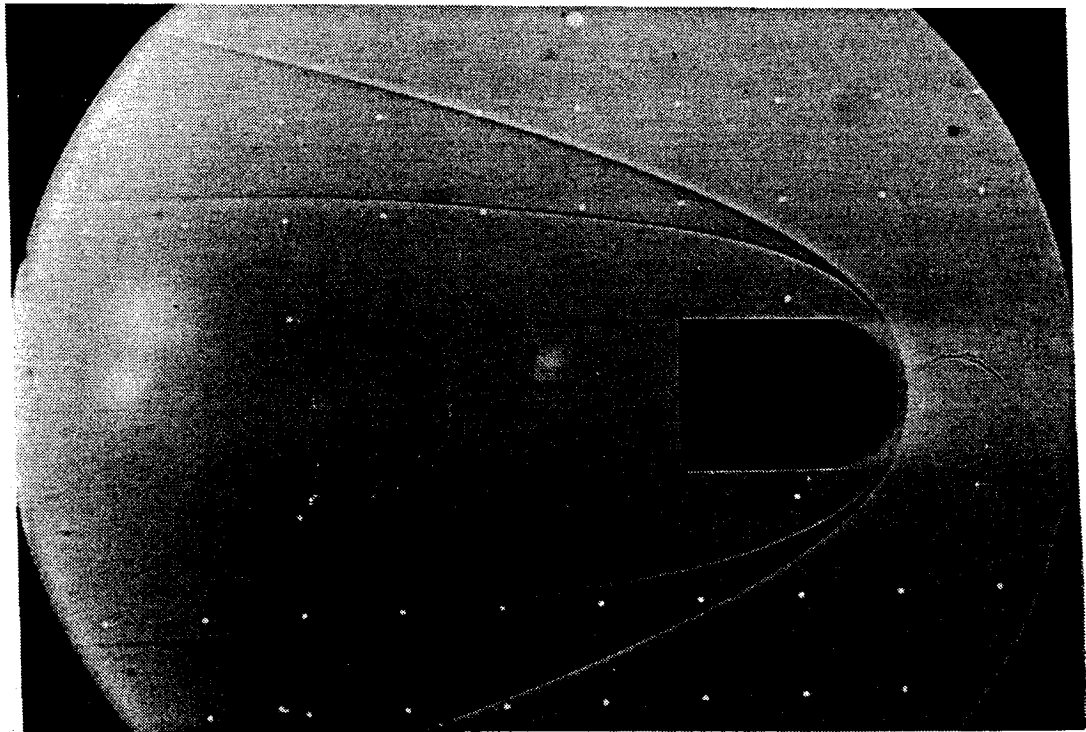
Figure 2 Shadowgraph of a spherical nose projectile moving at
Mach 6.46 into a premixed stoichiometric hydrogen-air mixture.
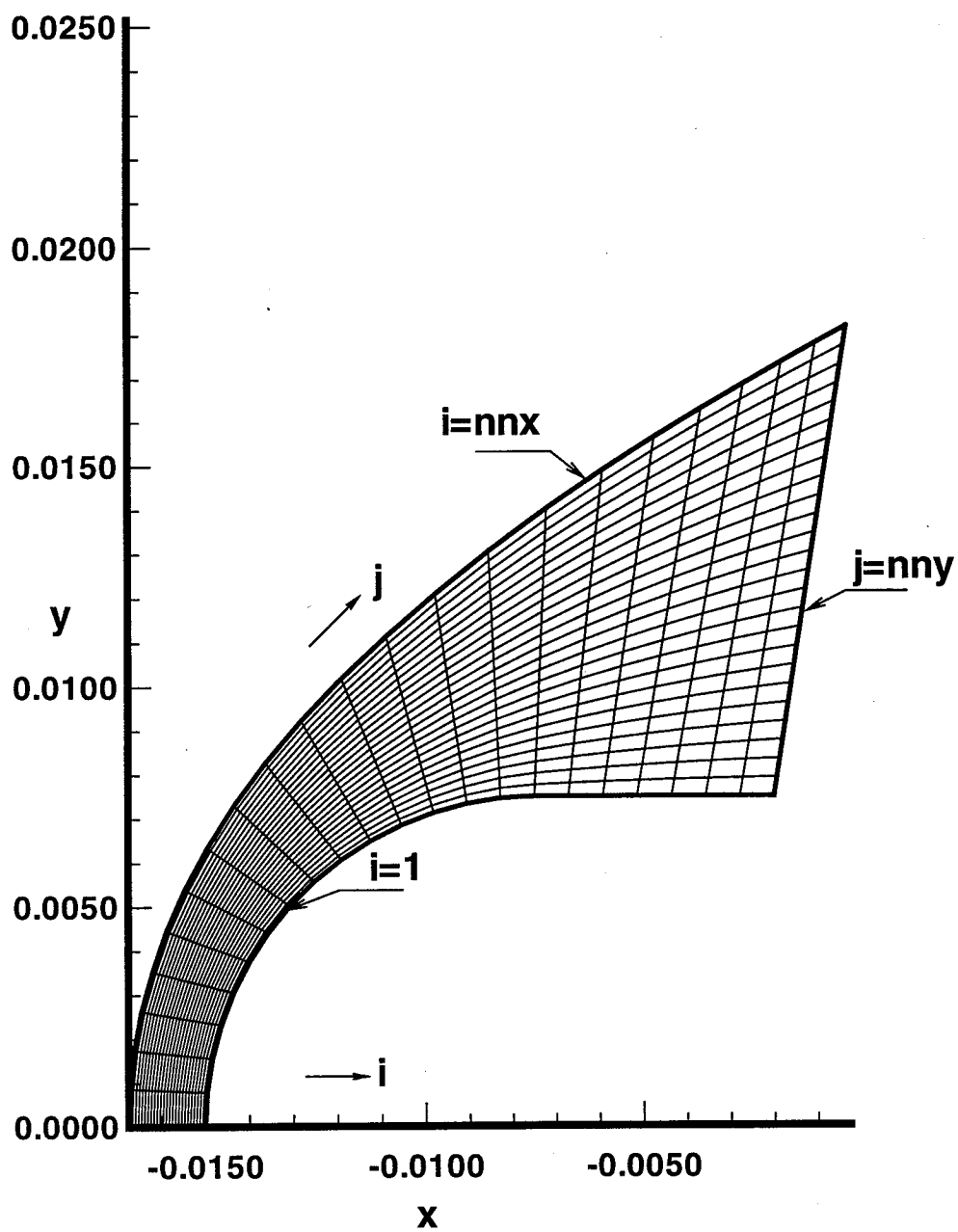
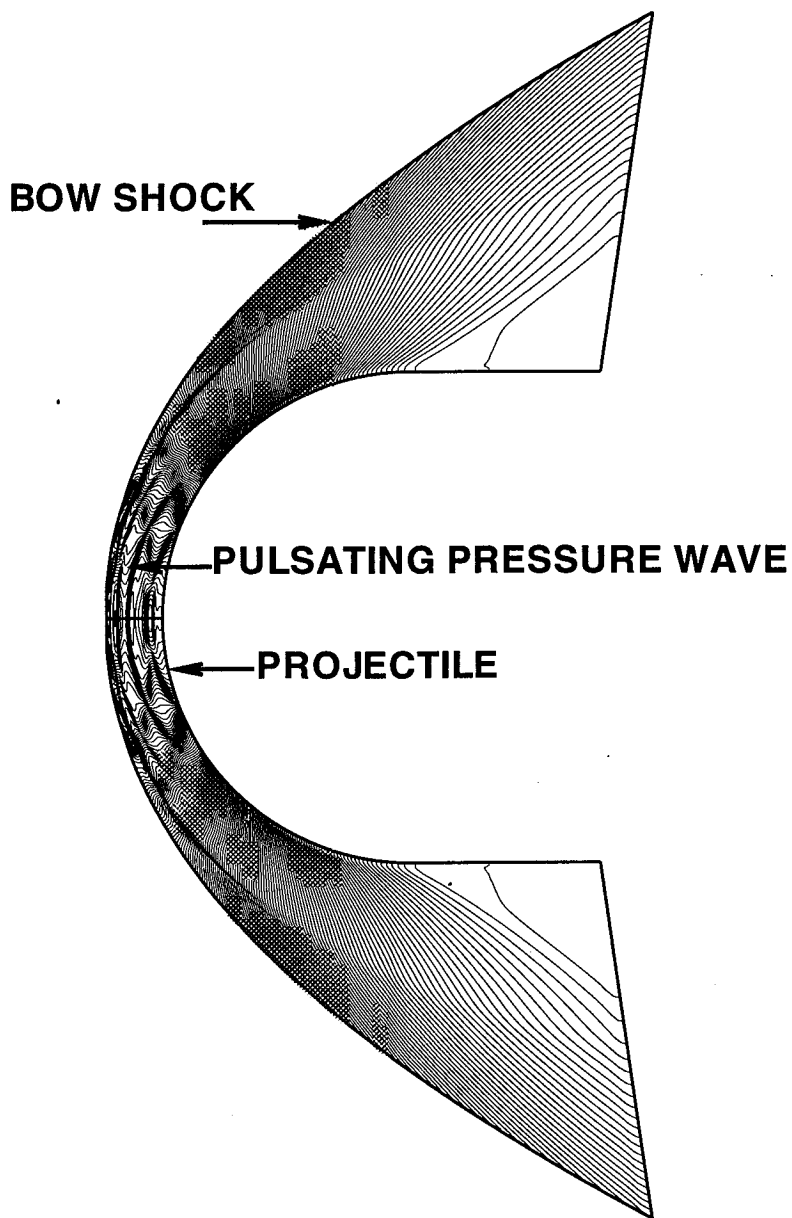Figure 4 Typical grid used in the computation (every 4th point shown)

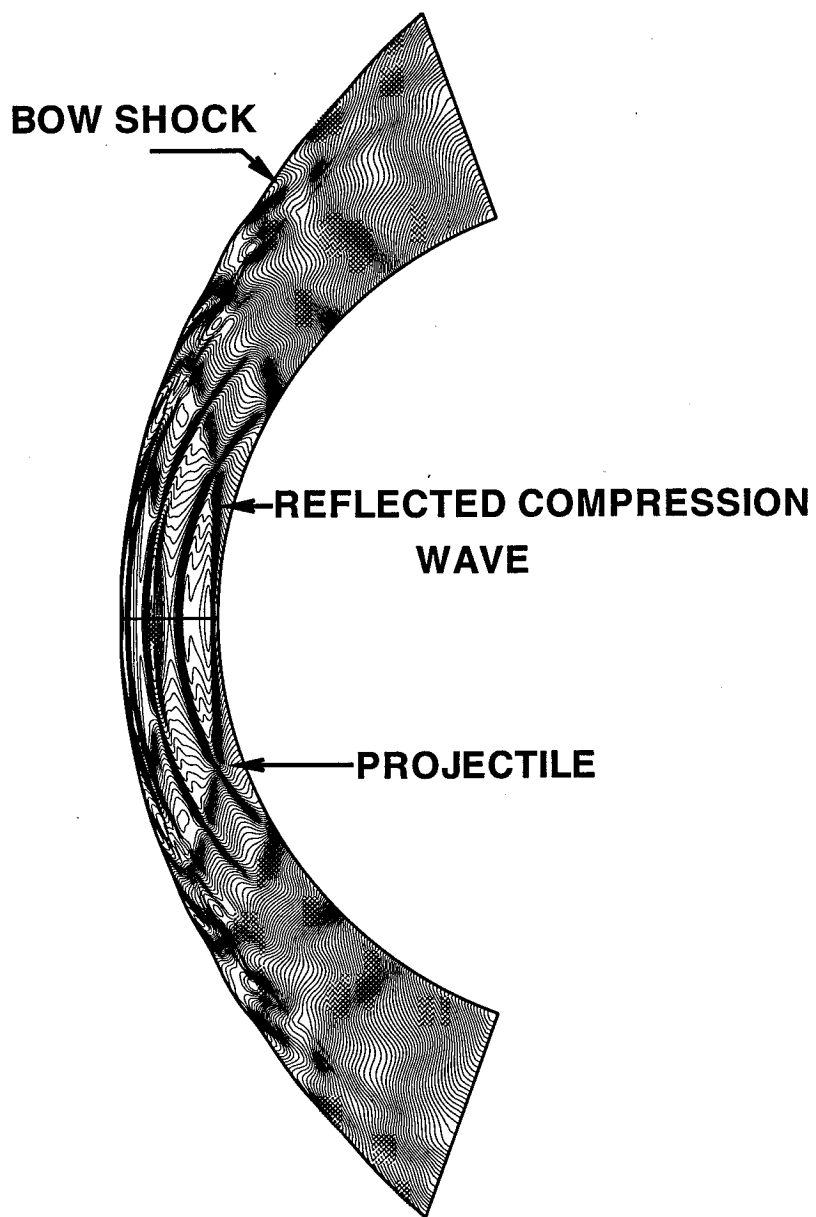Figure 5 Pressure contours for Mach 5.11 case
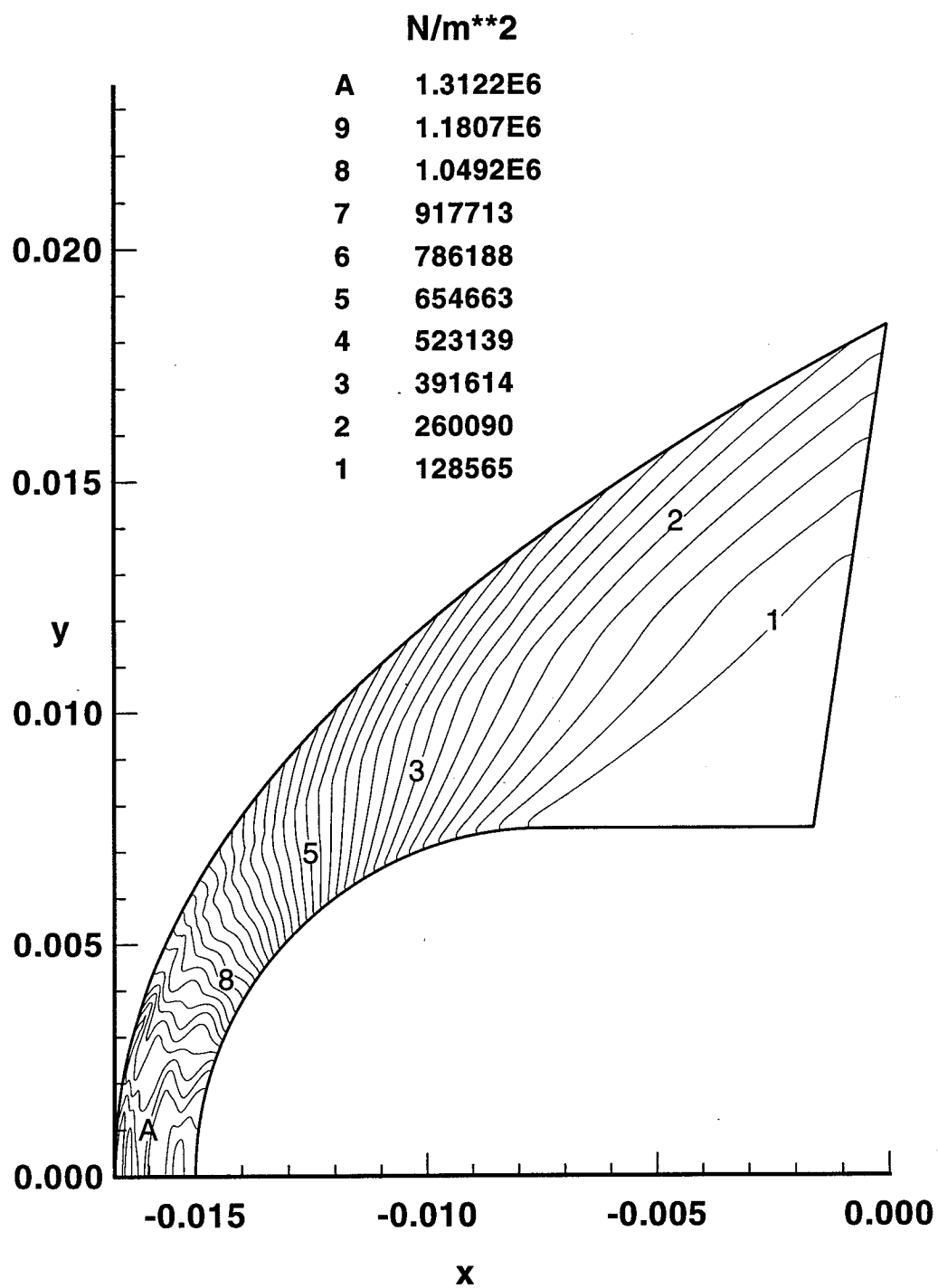
Figure 6 Enlarged pressure contours for Mach 5.11 case

N/m**2

	N/m**2
A	1.3122E6
9	1.1807E6
8	1.0492E6
7	917713
6	786188
5	654663
4	523139
3	391614
2	260090
1	128565

Figure 7 Pressure contours showing numerical pressure distribution
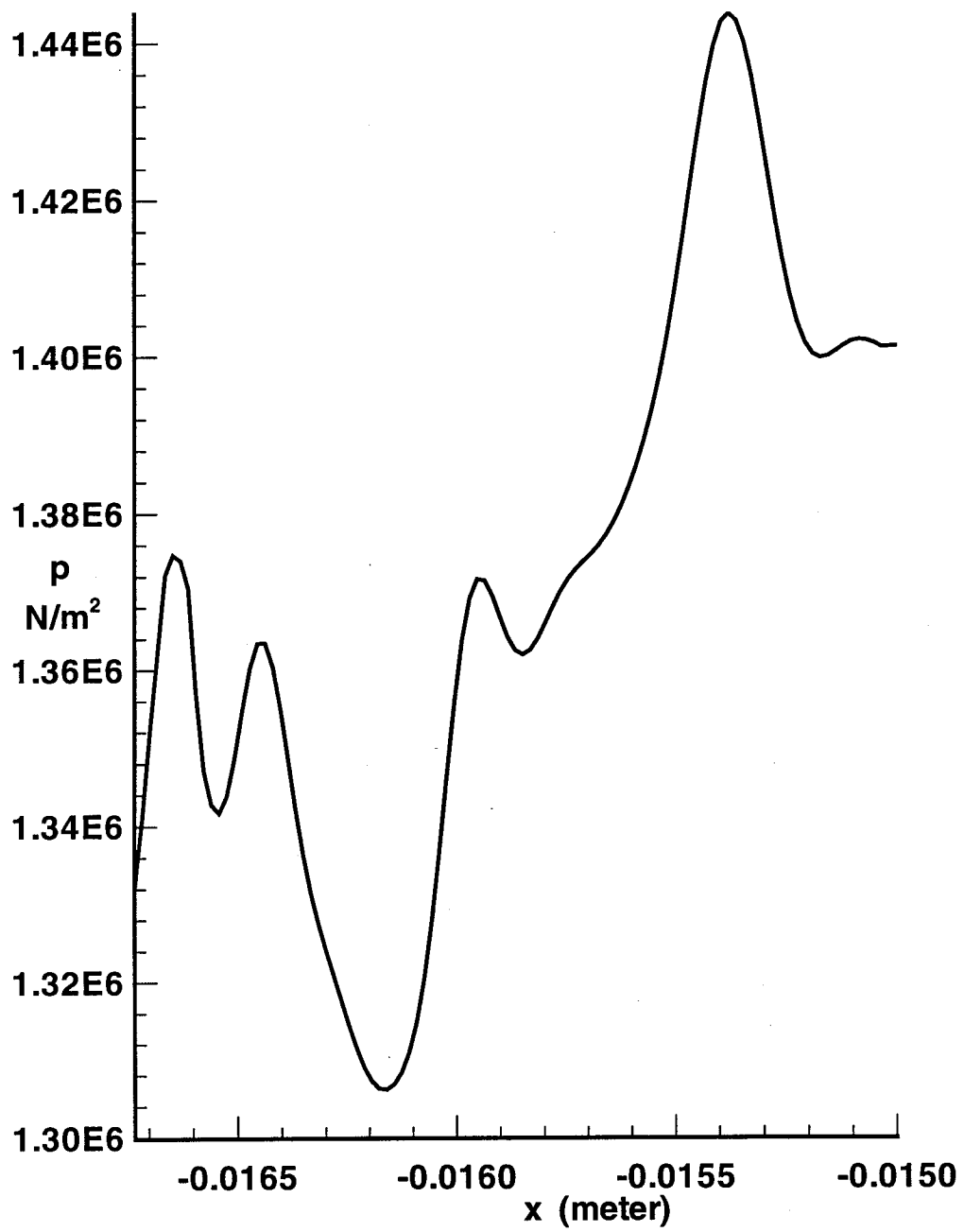
Figure 8 Pressure distribution for Mach 5.11 along stagnation streamline
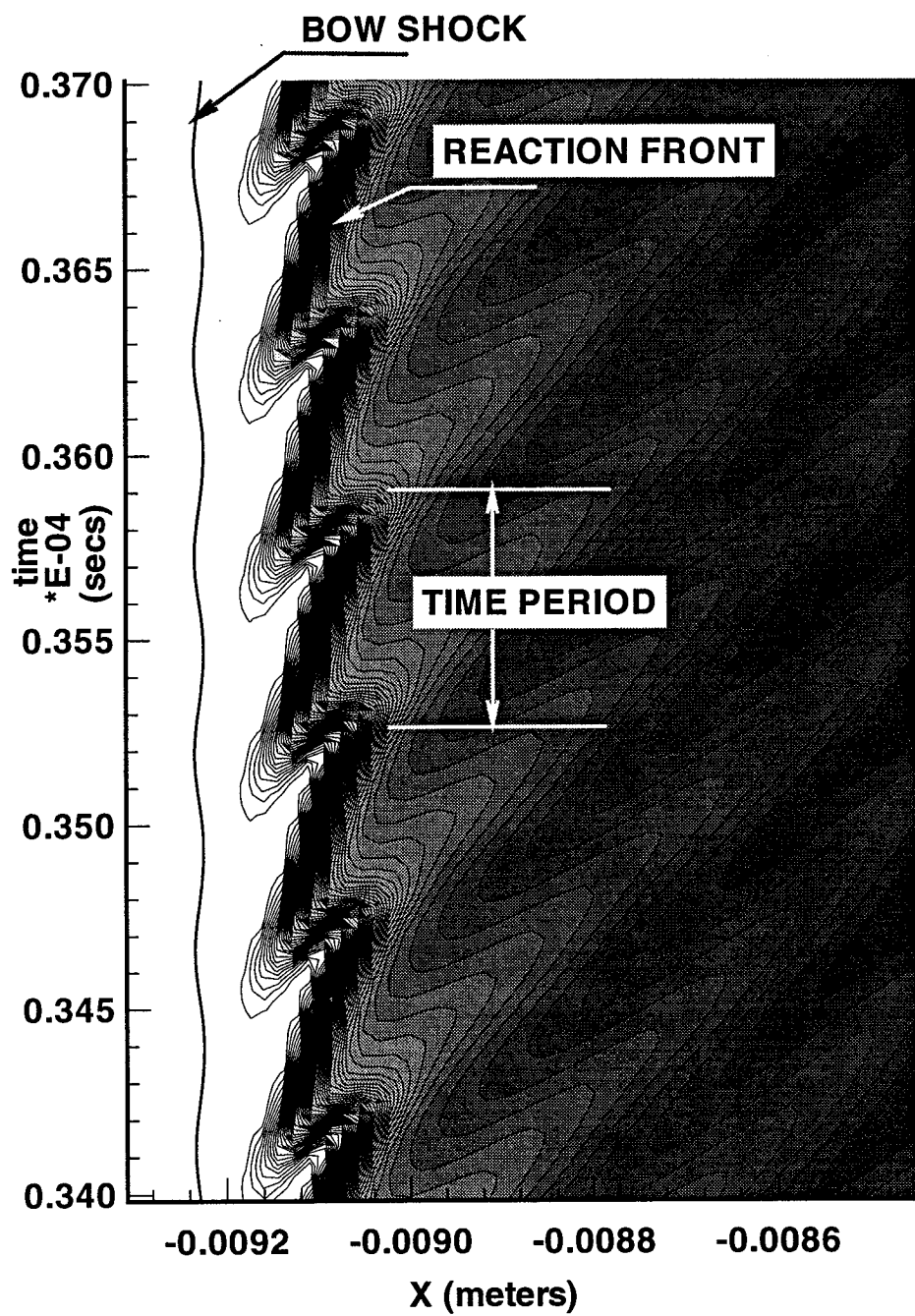
Figure 9 Time history plot of water mass fraction for Mach 5.11

REACTION FRONT

A	0.196772
9	0.17525
8	0.153728
7	0.132206
6	0.110684
5	0.0891622
4	0.0676403
3	0.0461184
2	0.0245965
1	0.00307456
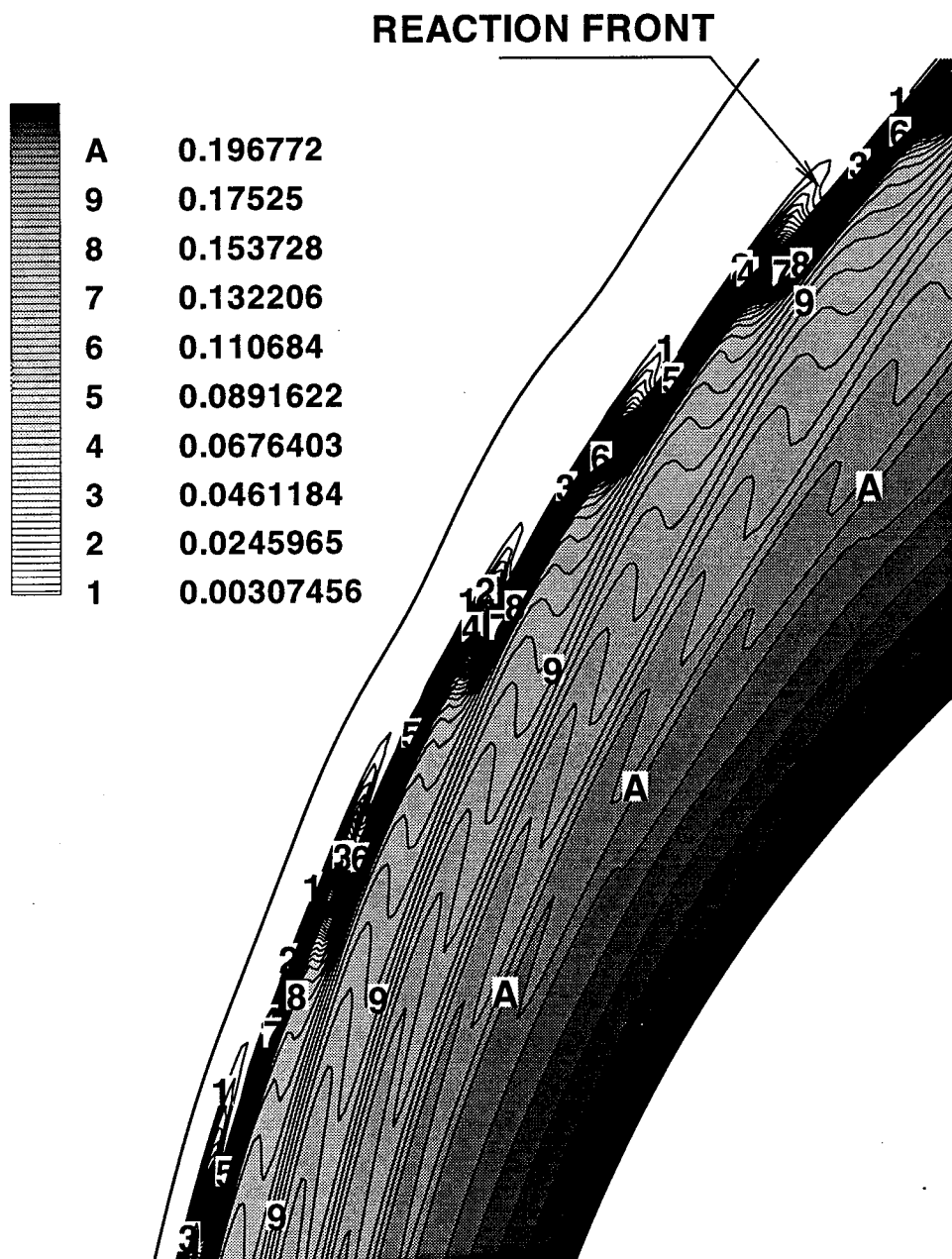
Figure 10 Water mass fraction contours for Mach 5.11

A	2.08187
9	1.88499
8	1.68812
7	1.49124
6	1.29436
5	1.09749
4	0.900612
3	0.703735
2	0.506859
1	0.309983
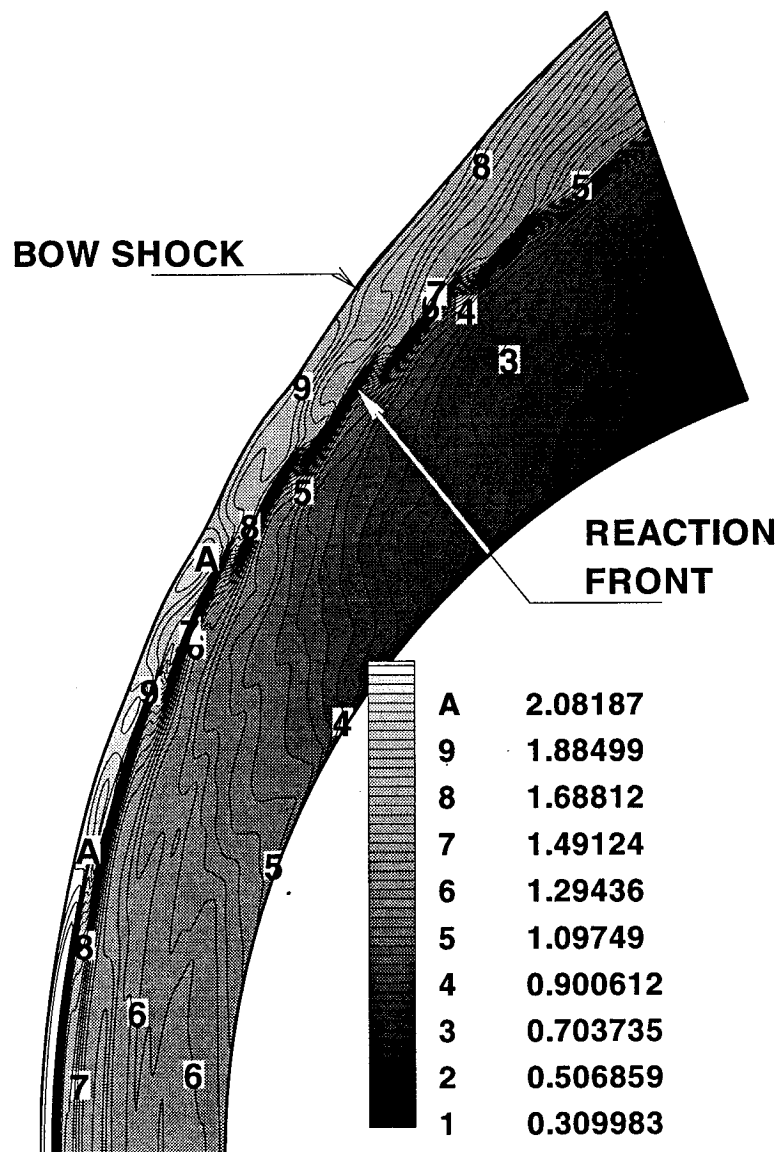
Figure 11 Density contours for Mach 5.11
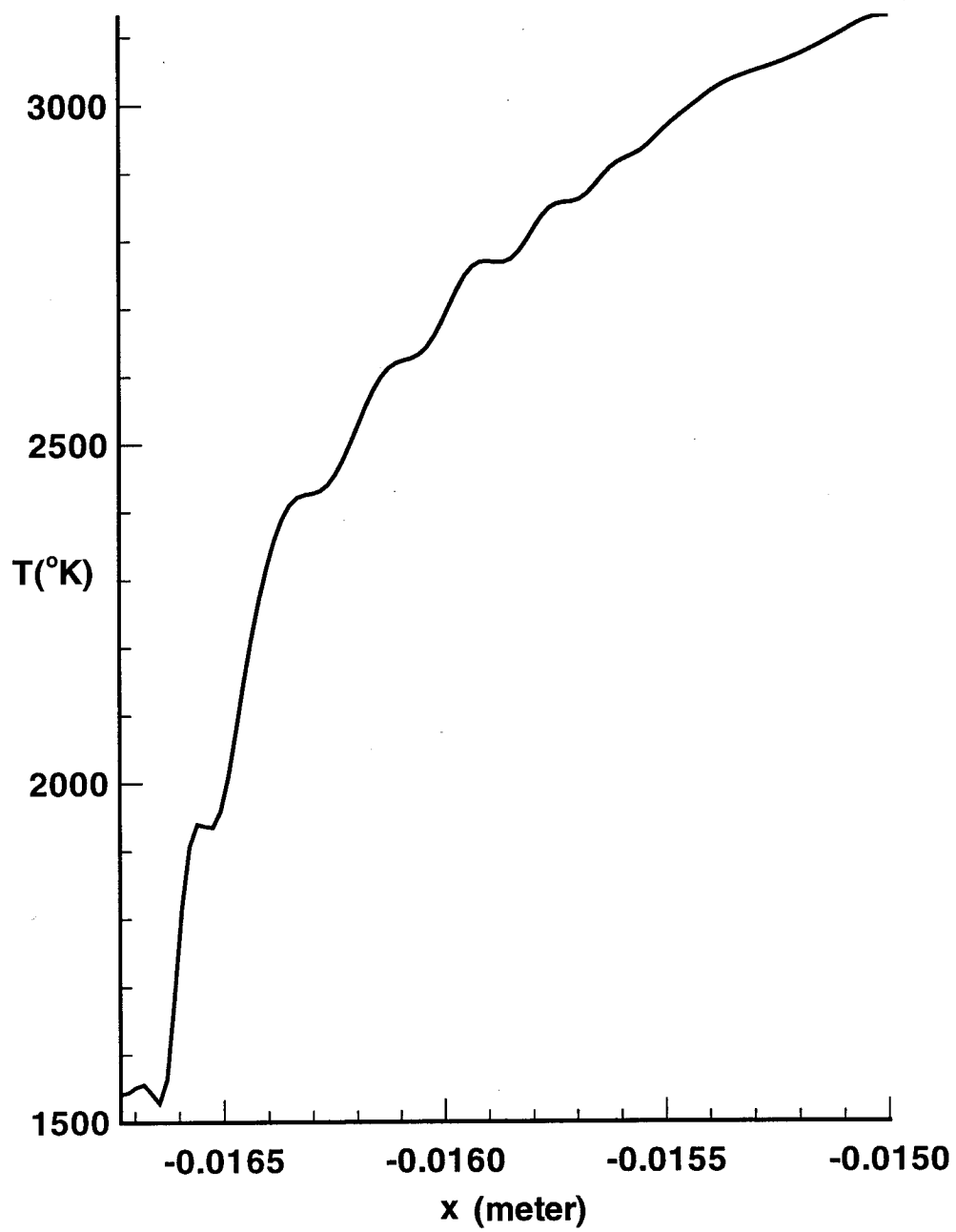
Figure 12 Temperature distribution along stagnation streamline for Mach 5.11

BOW SHOCK

REACTION FRONT

PROJECTILE SURFACE
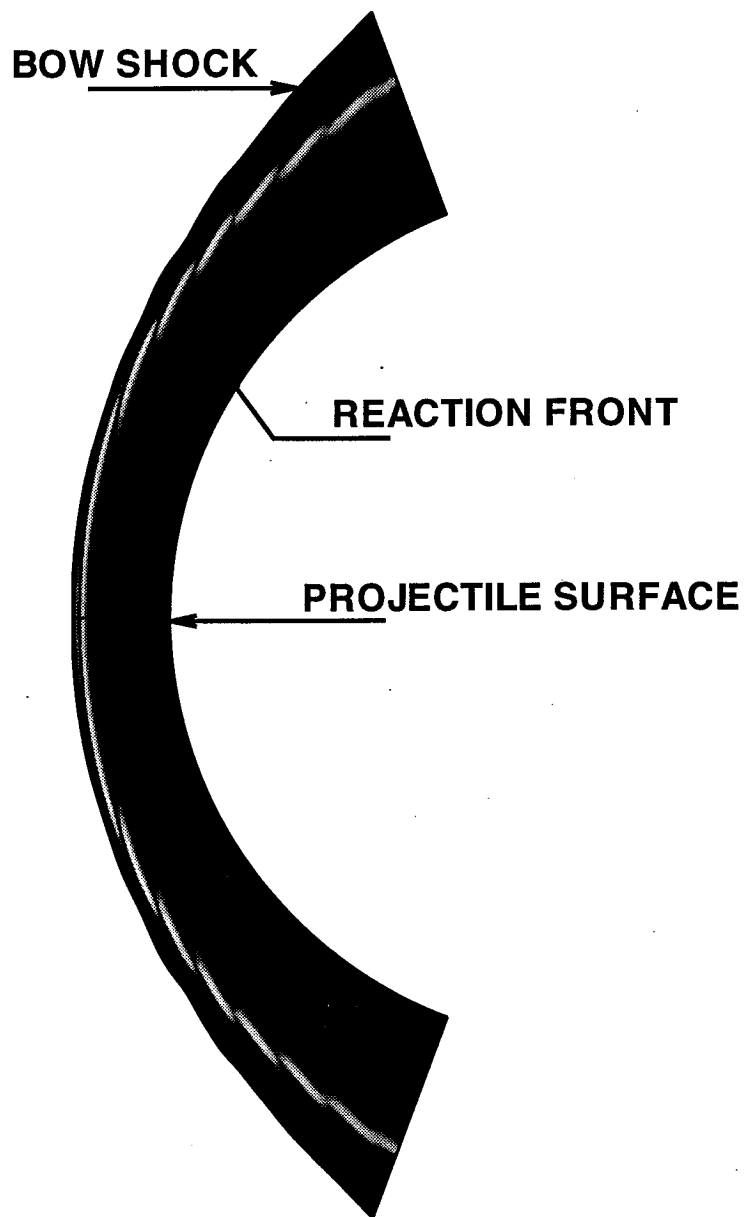
Figure 13 Computed shadowgraph for Mach 5.11
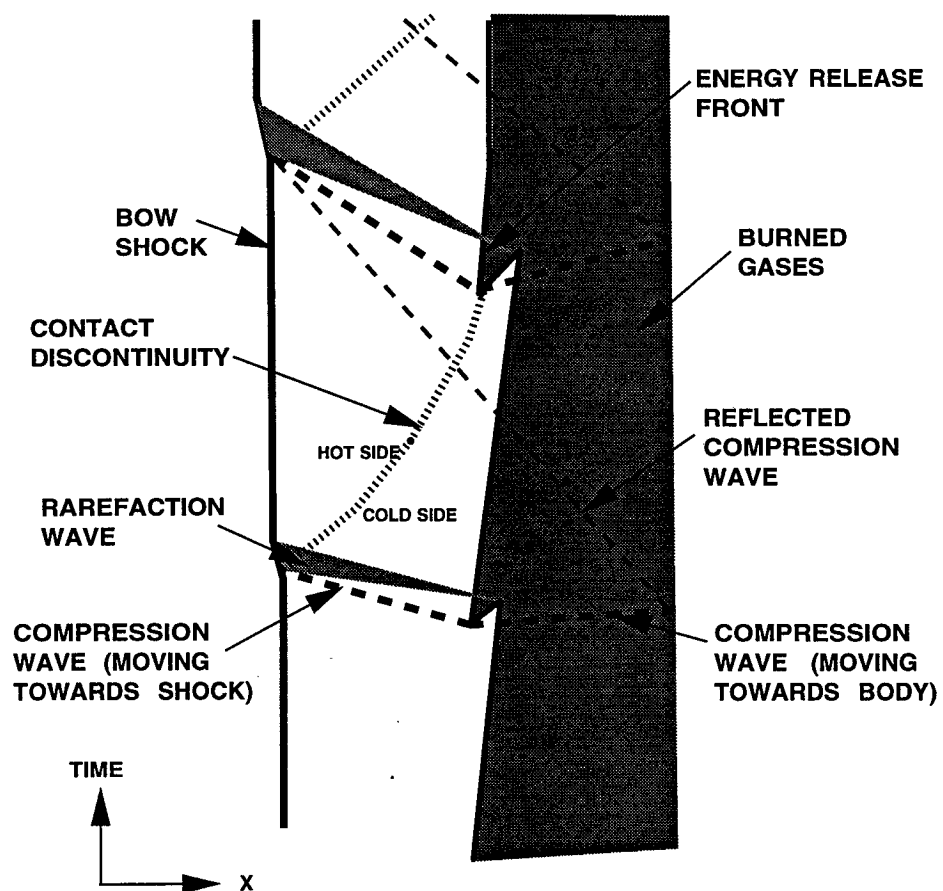
Figure 14 One dimensional wave interaction model

BOW SHOCK

REFLECTED

COMPRESSION WAVE

COMPRESSION WAVE
MOVING TOWARDS
PROJECTILE

PROJECTILE BODY

TIME

X
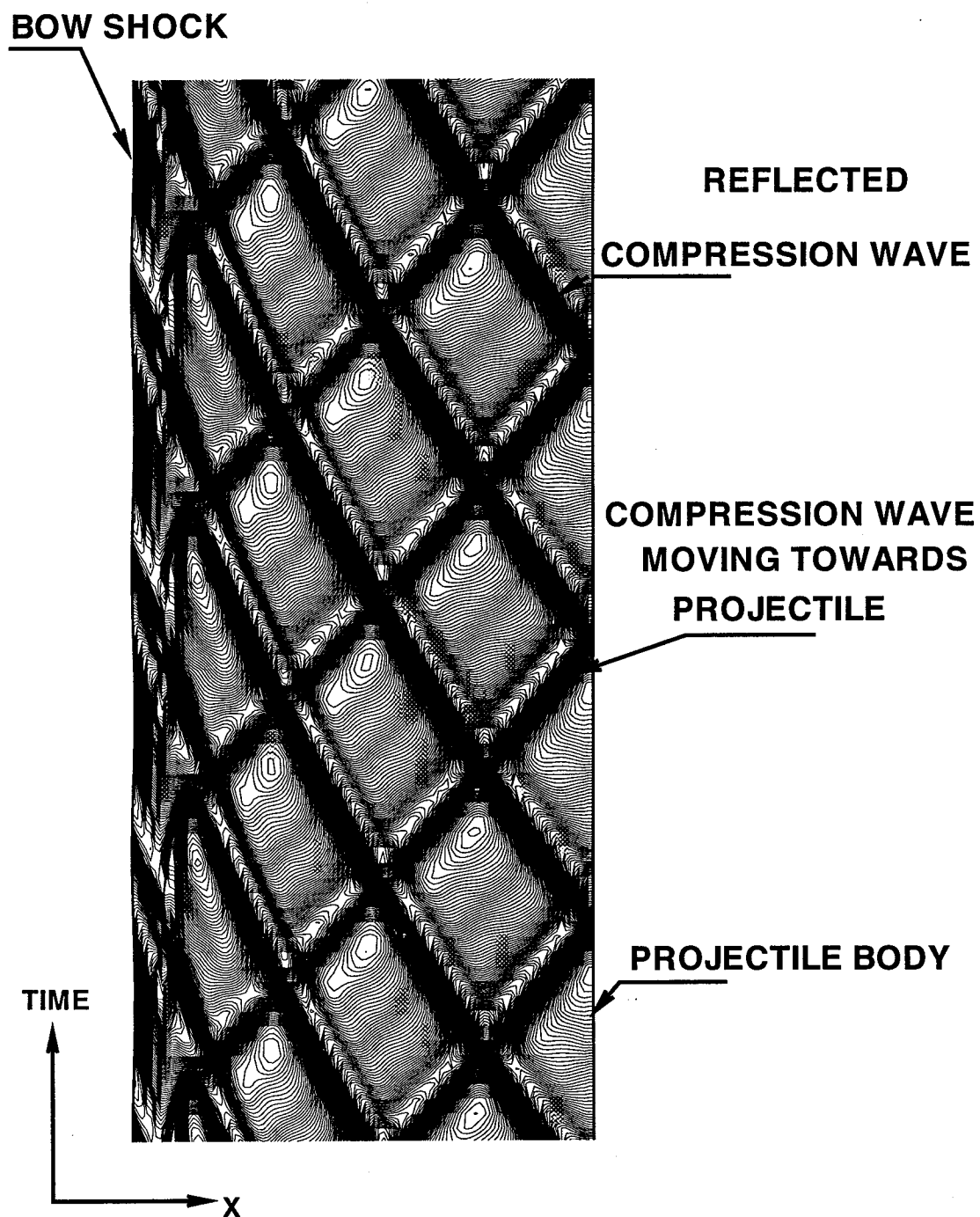
Figure 15 Time history plot of pressure along the stagnation line for Mach 5.11
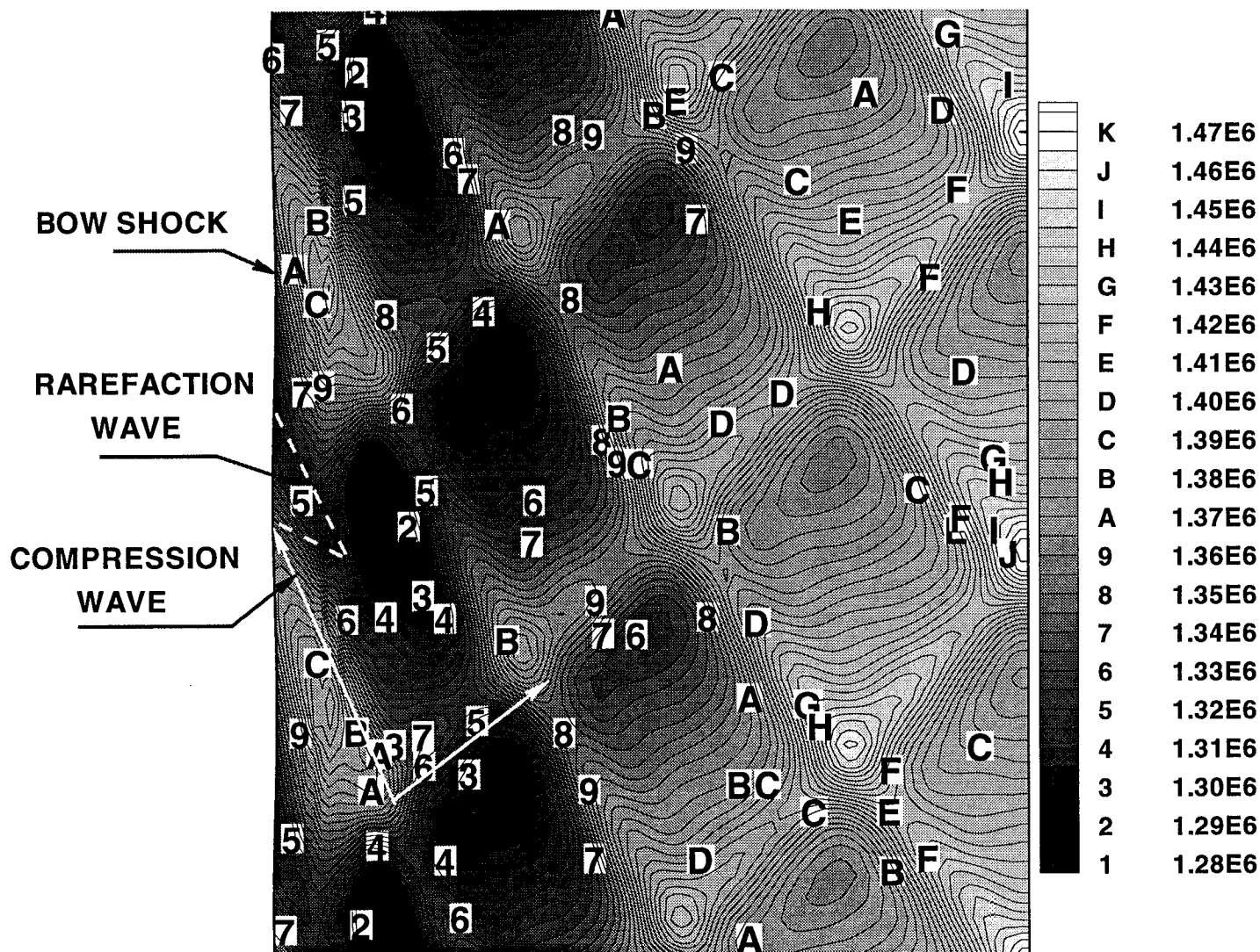
Figure 16 Time history plot of pressure along the stagnation line for

Mach 5.11 showing numerical values for pressure
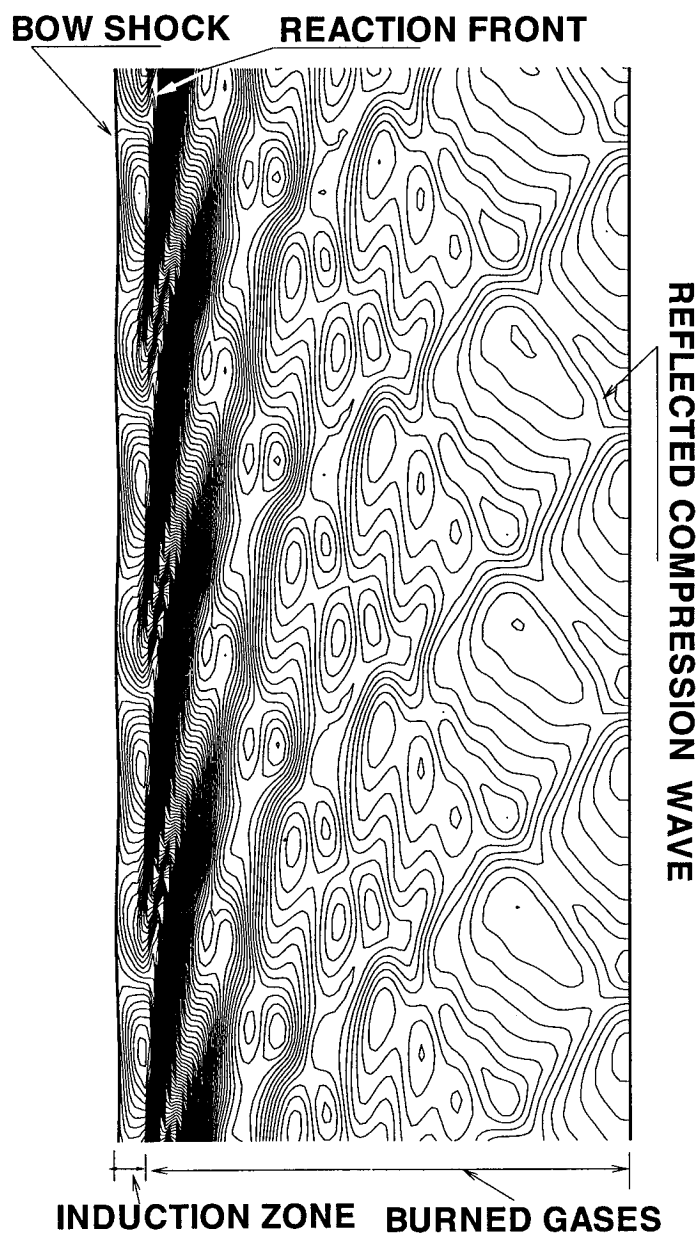
Figure 17 Time history plot of density along the stagnation line for Mach 5.11
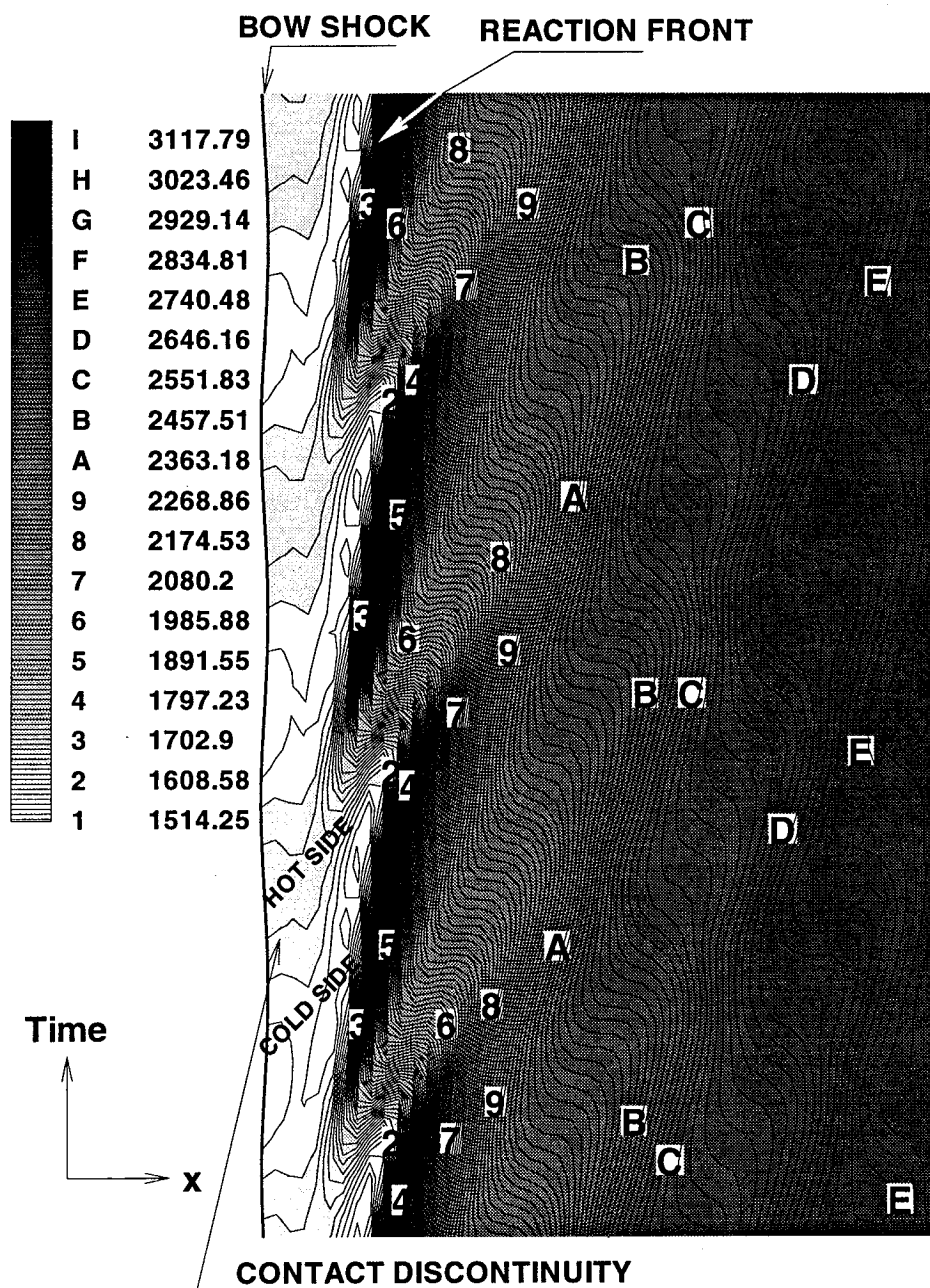
Figure 18 Time history plot of temperature for Mach 5.11

BOW SHOCK

REACTION FRONT

PROJECTILE SURFACE
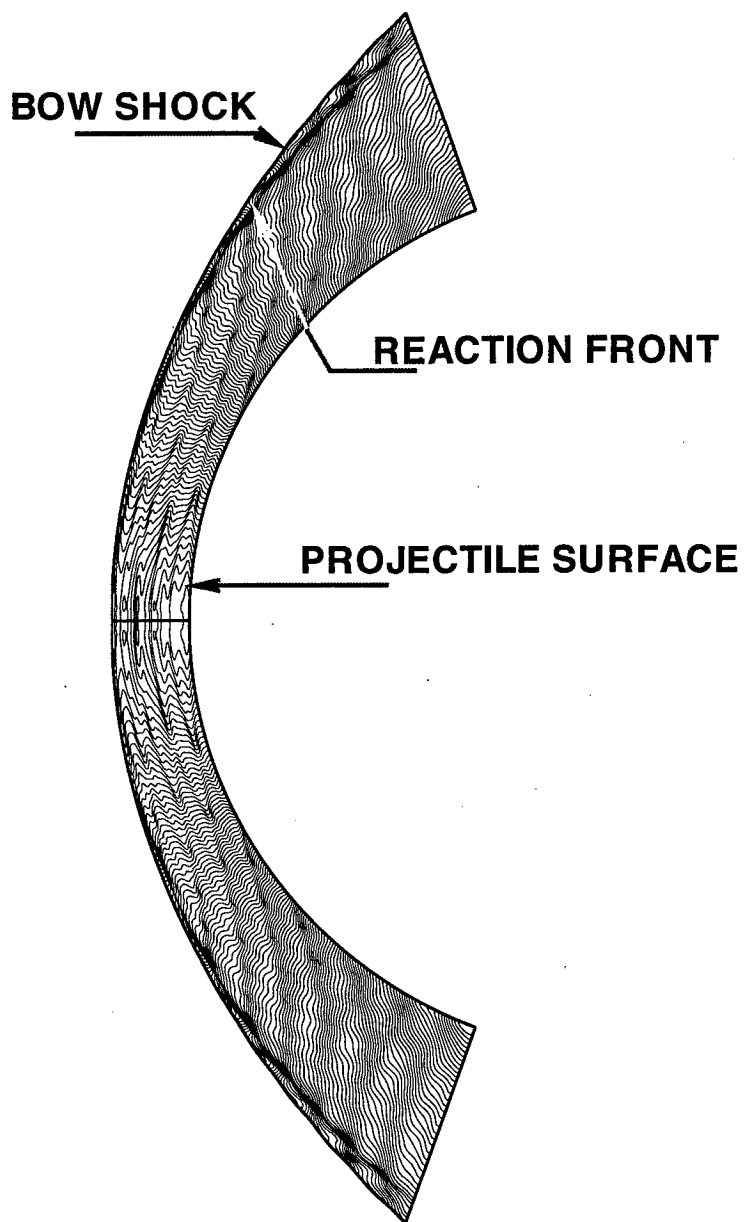
Figure 19 Pressure contours for Mach 6.46
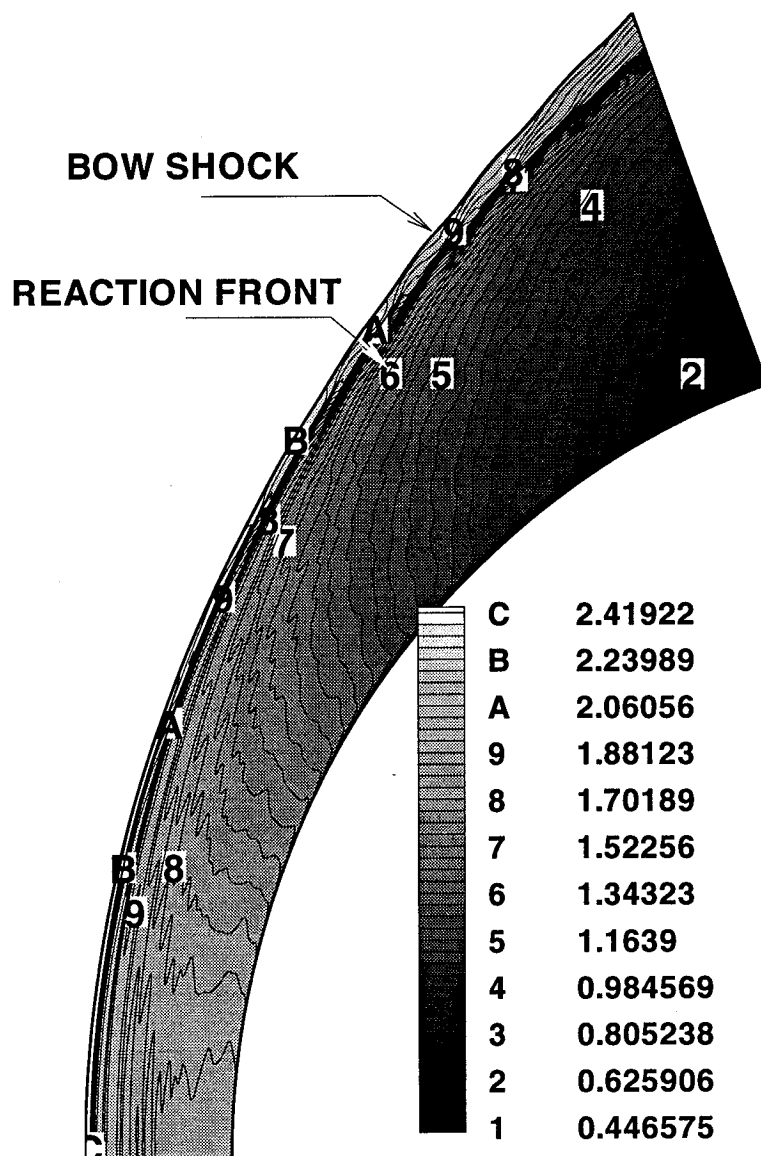
Figure 20 Density contours for Mach 6.46
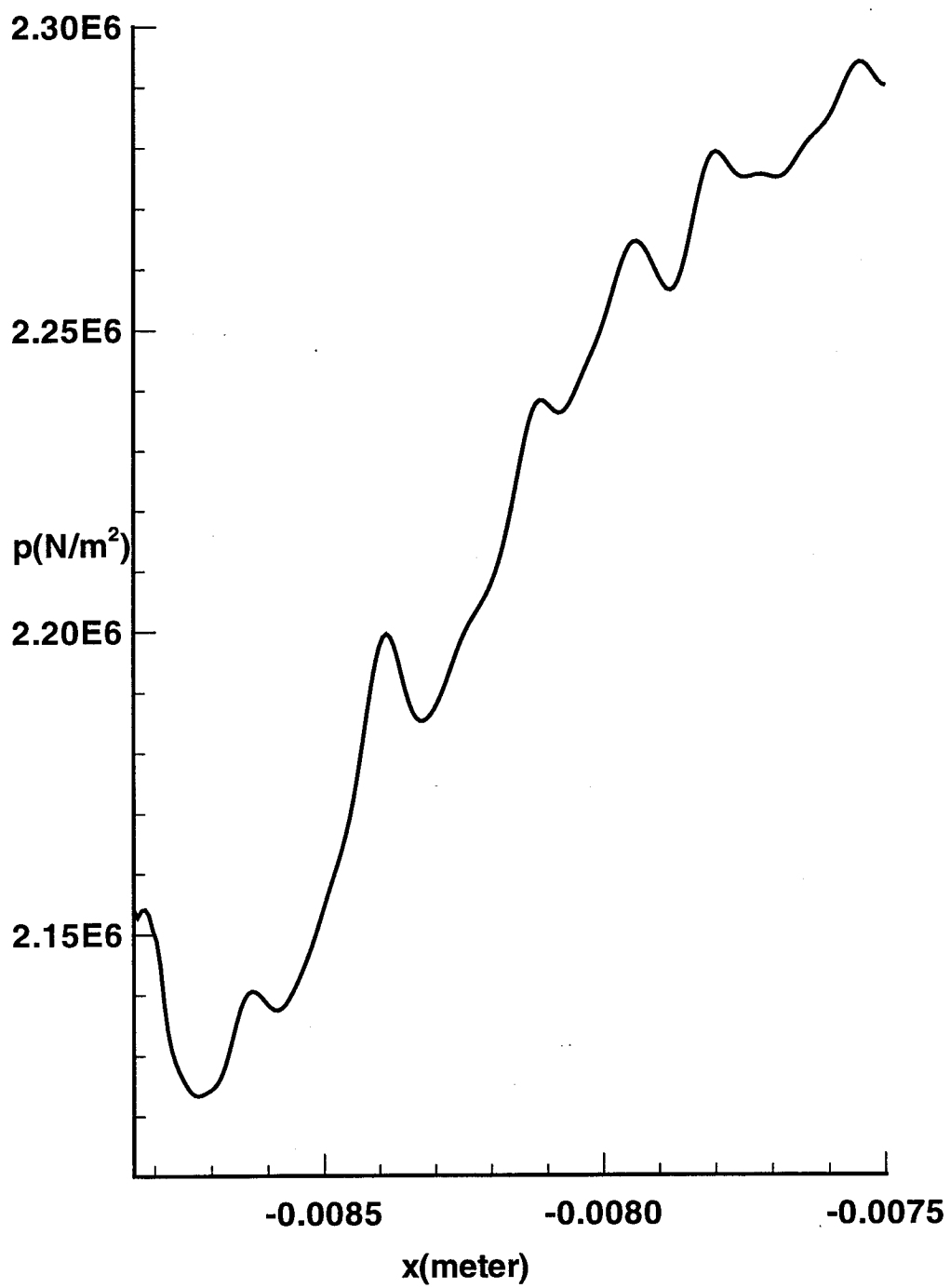
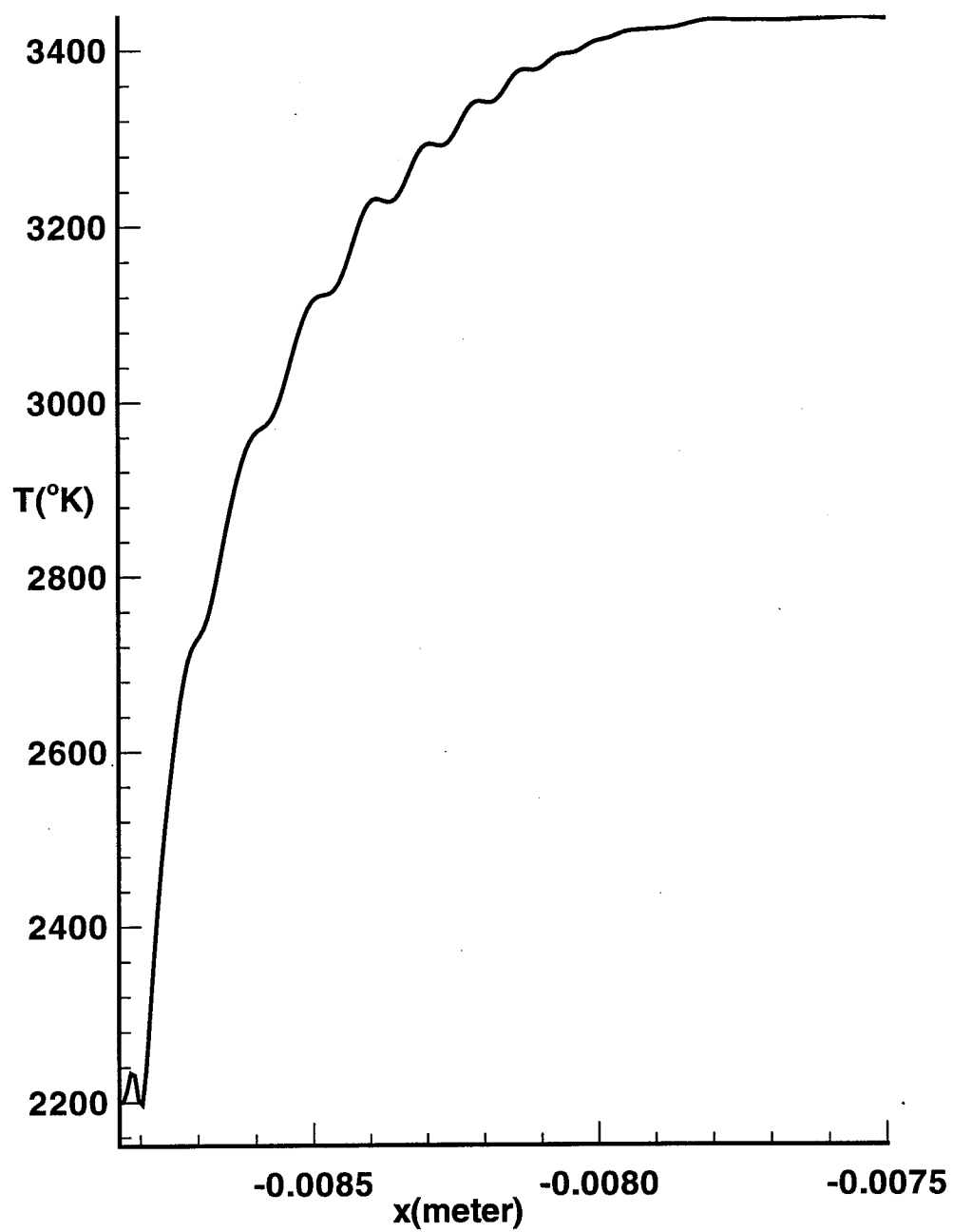Figure 21 Pressure distribution along stagnation line for Mach 6.46

Figure 22 Temperature distribution along stagnation line for Mach 6.46
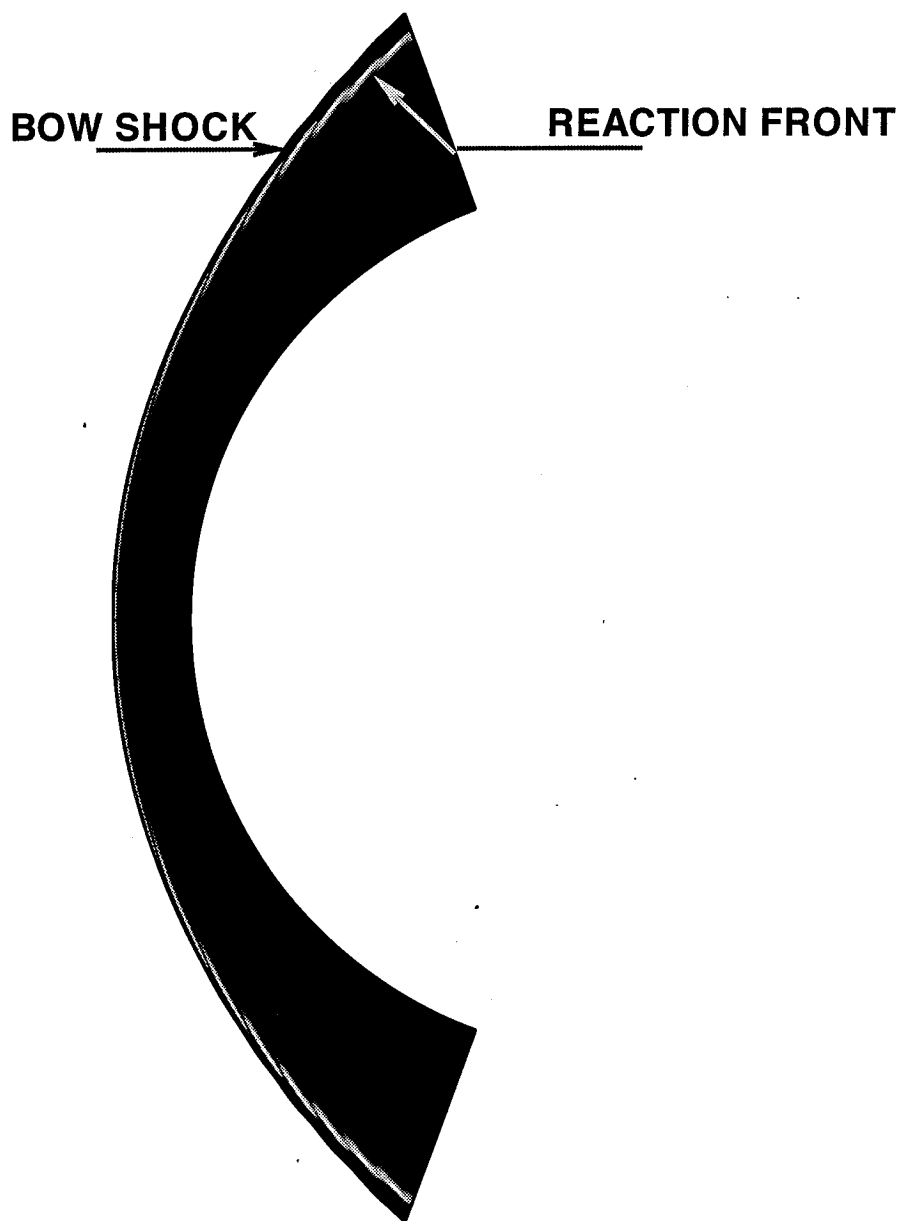
BOW SHOCK　　　　　**REACTION FRONT**

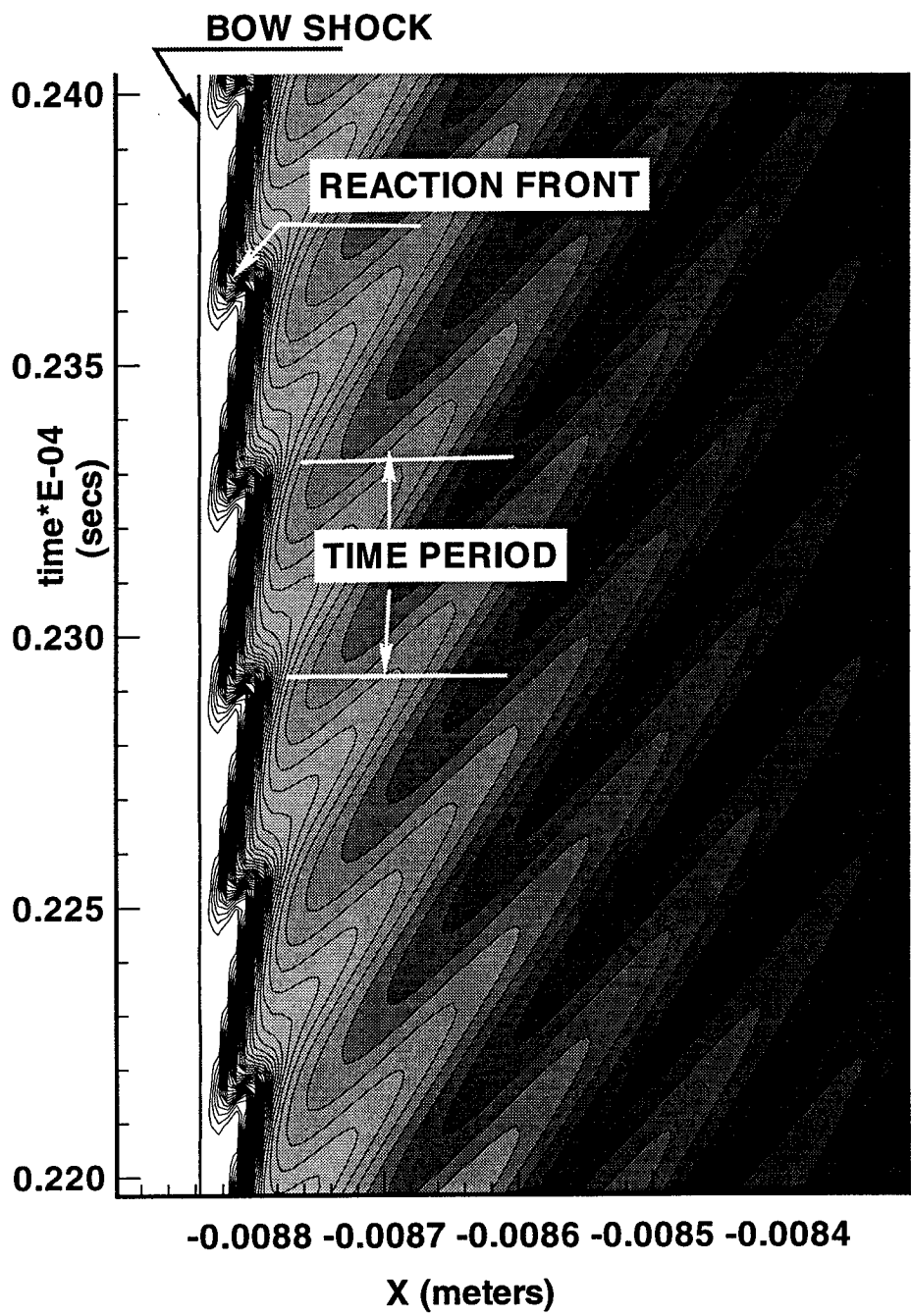Figure 23 Computed shadowgraph for Mach 6.46

Figure 24 Time history plot of water mass fraction along stagnation line for Mach 6.46